Design standardisation and seismic protection of SMRs through modular metafoundations

Tugberk Guner [a], Chiara Nardin [a], Oreste S. Bursi [a,*], Silvano Erlicher [b], Alexandre Monteil [c]

[a] *Department of Civil, Environmental and Mechanical Engineering, University of Trento, 38123, Trento, Italy*
[b] *EGIS Business Unit, Major Structures, Water, Environment, Energy rue Dolorès Ibarruri, TSA 50012 - 93188 Montreuil, France*
[c] *Civil Engineering NI Design for EDF SMR Project, EDF – DIPNN – DT Civil Eng. Team, 19 rue Pierre Bourdeix, 69007 Lyon, France*

ARTICLE INFO

ABSTRACT

This paper investigates the seismic protection of the Nuward™ small modular reactor (SMR) building, focusing on design loading and beyond design basis earthquake (bDBE) conditions. The study aims to achieve two primary objectives: i) to enhance seismic mitigation of a SMR building under bDBE conditions, through the use of the innovative modular single-layer (SLM) and multi-layer (MLM) metafoundations (MFs); ii) to effectively standardise and harmonise SMR building designs in locations prone to beyond design basis conditions. To accomplish these goals and demonstrate the protective capabilities of the MFs, the study employs non-linear time-history analyses (NLTHAs) for both DBE and bDBE conditions. Along these lines, a reduced-order model was developed from a refined finite element (FE) model of the SMR building using the Craig-Bampton mode synthesis technique. Then, finite locally resonant modular MFs were designed and analysed using NLTHAs. Specifically, physics-based ground motion models (GMMs) were used to generate and select seismic triplets that mimicked DBE and bDBE scenarios for NLTHAs. Successively to achieve improved seismic performance, the optimization of the MFs was pursued by targeting the optimal number of columns, resonator parameters, and unit cell dimensions. Additionally, the deployment of inerters was considered, to significantly reduce the size of the MFs and enable their application in multiple layers for ultra-low frequency attenuation. The overall findings suggest that modular MFs meet seismic protection requirements, and positively contribute to the standardization process of SMR buildings, even in areas characterized by beyond-design seismic conditions.

1. Introduction

1.1. Background

The research on the aftermath of the 2011 Fukushima earthquake (Stevenson, 2014) revealed nuclear power plant (NPP) resilience to earthquakes. However, subsequent tsunami flooding, triggered by 13–14 m waves, caused severe damage, releasing radiation (IAEA, 2016). Hence, the Fukushima disaster demonstrated the importance of a more robust and intrinsically safe NPP design. Notably, it focused on the critical need to account for cascading effects and compounding repercussions in maintaining overall NPP safety. This emphasized the importance of going beyond typical state-of-the-art design approaches. Moreover, in response to growing energy demand and global efforts for net-zero emissions, many countries actively invest in green energy, particularly emphasizing nuclear power. However, large NPPs require 5–10 years of construction, a multi-billion dollar investment and they are often delivered over budget and over time. Therefore, the interest towards small modular reactors (SMRs) is rapidly increasing (Mignacca et. al., 2020). Along these lines, over 50 SMR designs and concepts are in development (IAEA, 2020). Among them, the NuWard™ SMR, developed by an EDF-led consortium in France, offers 340 MW(e) via two independent reactor modules within a compact SMR building.

Thanks to their compact and advanced designs, SMRs present advantages in terms of safety, quality, power scalability, and economic affordability (Upadhyay et al., 2003). Regarding seismic resilience, Di Maio et. al. (2023) showed that SMRs exhibit greater resilience compared to conventional NPPs. SMRs also represent an ideal opportunity to gain access to clean energy from low-emission sources, for geographical regions with underdeveloped infrastructure. Along these veins, the modularization and standardization of the SMR designs is of paramount importance. In particular, improving the design and

---

construction strategies of SMRs unlocks safer and more reliable deployment and maintenance practices. Specifically, one of the main challenges of standardization concerns seismic protection.

Historically, the seismic input was defined as a generic smooth ground response spectrum (GRS), such as the 5 %-damped median NUREG/CR-0098 (U.S. Nuclear Regulatory Commission, 1978) response spectrum. However, generic – i.e., no site –based spectra are not appropriate for regions where the representative response spectral shapes are significantly different over the frequency of interest, see Cai et al. (2018). In this respect, current codes and standards allow the designer to consider three acceleration time histories in mutually orthogonal directions, i.e., two horizontal directions, H1 and H2, and one vertical direction V, as in USNRC SRP 3.7.1 (U.S. Nuclear Regulatory Commission, 2014a) and CSA N289.3 (CSA, 2010). Nevertheless, the generated tri-directional seismic time series must meet strict code requirements, thoroughly discussed in the literature review work of Ni et al. (2011) and Yang et al. (2021). In particular, the primary code requirements demand: (i) compatibility of the two horizontal and one vertical time series with target ground response spectra S_{H1}^T, S_{H2}^T and S_V^T, respectively; (ii) statistical independence between each pair of time histories; (iii) smooth and controlled variation of the Arias Intensity feature for the ground motions, and, (iv) no baseline drift for the derived displacement time histories. Natural triplets that fulfil all the above-mentioned requirements are difficult to retrieve from historical datasets, especially in the number needed for assessing the performance of the coupled 3D system. Hence, ground motion models (GMMs) have proved to be effective for generating horizontal and vertical ensembles of synthetic time histories from which to extract code-compliant synthetic triplets.

A common seismic protection solution of structural systems consists of base isolation, which is capable of uncoupling a superstructure, the SMR building in this particular case, from the ground. In this respect, several numerical and experimental activities have been conducted by Zhao et al., (2019) and Schellenberg et al. (2015), among others. Besides, to favour the linear behaviour of laminated rubber bearings, the Japanese technical guidelines (JEAG4614, 2013) suggest safety margins to be used in strong earthquake-prone zones. In this respect, Parsi et al. (2022) promoted the standardization of advanced reactor designs based on seismic isolation and demonstrated two different advanced reactors based on molten salt and high-temperature gas, respectively. However, whilst these solutions effectively mitigate horizontal seismic actions, no protection against vertical actions is offered. Additionally, seismic isolation devices necessitate precise gravity load distribution, posing another challenge for design standardization. Therefore, to satisfy seismic protection against both vertical and horizontal excitations, Fukasawa et al. (2019) proposed a new 3D complex isolator consisting of rubber bearings, vertical oil dampers and disc spring units. Similarly, Najafijozani et al., (2020) proposed six systems based on adaptive control. They consist of in-parallel springs and dampers with linear and nonlinear behaviour configurations. An updated and significant real-world example of 3D isolation has been studied and implemented by Nielsen et al. (2020) on the Loma Linda University Medical Center Replacement Hospital. The proposed solution integrated traditional triple friction pendulum isolators with large stroke fluid viscous dampers, alongside a novel vertical isolation system comprising steel pedestals, helical coil springs, fluid viscous dampers, and low friction sliding shear pins. Anyway, it is crucial to note that the introduction of vertical and horizontal flexibilities, as emphasized by Medel-Vera and Ji (2015), may necessitate a rocking suppression system for 3D isolation. In light of these findings, drawbacks of isolation devices include: (i) the need for intricate mechanical solutions for vertical isolation and rocking suppression; (ii) frequent and diverse maintenance needs, and (iii) a high likelihood of failure due to rubber decay or friction surface wear. Thus, these shortcomings render conventional isolation solutions unsuitable for fulfilling one of the primary purposes of SMRs: achieving a modular and standardised design.

Recently, a great deal of attention has been given to metamaterials as a novel approach for seismic vibration mitigation. In particular, metamaterials are characterised and designed by engineered properties not found in nature. Unlike traditional materials, metamaterials derive their characteristics from specially engineered periodic structures rather than material's intrinsic properties. Their properties and applications have earned them a place on Materials Today's list of top 10 advances over the past 50 years (Wood, 2008). In the fields of structural and mechanical engineering, metamaterials are explored for their potential in impact resistance (Wu et al., 2020) and vibration control (Ji et al., 2021; Dalela et al., 2022). Moreover, locally resonant metamaterials (LRMs), a distinguished class of metamaterials, utilize localized resonances to manipulate specific frequency ranges (Ma and Sheng, 2016). By incorporating resonant elements, LRMs can selectively attenuate or amplify certain frequencies with reduced size. Therefore, LRMs show great potential for seismic protection, forming the basis of seismic metamaterials (Mu et al., 2020; Brûlé et al., 2020) that improve structural resilience and mitigate earthquake damage. Thus, they effectively dissipate seismic energy by leveraging localized resonances, integrating resonant elements strategically either along the paths between structures and seismic sources to counteract seismic waves (Zeighami et al., 2021) or within building foundations (La Salandra et al., 2017).

Using metamaterials as foundations, also known as metafoundations (MFs), offers a promising alternative for seismic protection in SMRs. Basone et al. (2019) investigated the use and benefits of MFs for protecting storage tanks against horizontal ground motions (GMs). Thus, optimized MFs with unit cells, which were conceived to be much smaller than the wavelength of the target frequencies, successfully mitigated low-frequency seismic waves. The effectiveness against vertical seismic waves was then verified by Franchini et al. (2020). In the context of NPPs, Guner et al. (2022) conceived a single-layer MF designed with reinforced concrete (RC) resonators and composite columns for the seismic protection of a NuScale SMR. To increase vertical flexibility, vertical quasi-zero stiffness layers were also proposed. The results revealed that MFs are effective against vertical/horizontal GMs but also to rocking motions, induced by augmented flexibility. However, the study was limited to 2D models and no in-depth investigation on the design standardization was carried out. Similarly, Witarto et al. (2019) conducted studies on seismic protection of SMRs by means of a periodic foundation. The Authors conceived a periodic foundation made of RC and polyurethane and attenuated waves in both the horizontal and vertical directions together with the torsional mode. They verified the periodic foundation experimentally on a shaking table with a 1/22 scaled mock-up. Clearly, the scaling reduced the potential problems of polyurethane layers.

One of the critical limitations of MFs is that heavy resonators are required to achieve proper protection. Likewise, the abovementioned studies demonstrated that the number of layers and resonator volumes are restricted due to limited space and cost. Thus, inerters, which provide a force response proportional to the relative acceleration between its two terminals (Smith, 2002), can be a perfect candidate to amplify the inertia of the resonators without increasing their physical mass/volume. In fact, one of their significant advantages is that their inertance can be multiple orders of magnitude higher than the actual mass. In structural control, the use of inerters for seismic protection has been proposed by several authors; see, for instance, the work of Ma et al., 2021 and Liu et al., 2022. Moreover, Watanabe et al. (2012) conducted experiments involving a full-scale tuned mass damper (TMD) with an inerter capable of generating 5400 tons of inertance from a 758 kg flywheel (amplification factor = 7124). As reported by Sugimura et al. (2012), this concept was subsequently applied to an actual steel structure in Sendai, Japan. Giaralis and his colleagues studied TMD with inerters and investigated the vibration suppression abilities against earthquake excitations (Marian & Giaralis, 2014). De Domenico et al. (2020) applied a tuned fluid inerter to a base-isolated structure. Both

studies showed that inerters could successfully reduce displacement demand on the isolators and base shear forces. Finally, Pietrosanti et al. (2021) conducted a shaking table testing campaign on a structure with a base isolation, TMD, and a rack-and-pinion flywheel-based inerter prototype, with a 95.6 kg of inertance starting from a 2.1 kg flywheel.

1.2. Motivation and scope

The research presented in this paper tackles two paramount aspects of the design and standardization of next-generation SMRs on these premises. First, it proposes the application of novel MFs with and w/o inerters, see Fig. 1, to overcome the drawbacks associated with conventional isolation solutions. Specifically, MFs overcome the (i) periodic maintenance, (ii) lack of adequate vertical protection, and (iii) complexity level of the design procedures and conventional isolators. Consequently, the performance of modular − single- and multi-layer − MFs with and w/o inerters for the seismic protection of the Nuward™ SMR building is deeply investigated. Secondly, to address the limitations of generic code spectrum prescriptions, a novel methodology for code-compliant triplets generation is developed. Specifically, it relies on physics-based GMM to generate the suite of ground motions and on the Hilbert-Schmidt Independence Criterion (HSIC) for the triplets selection.

The paper is structured as follows: Section 2 outlines the finite element (FE) modelling and accurate reduction of the Nuward™ SMR building model. The fundamentals of both MFs and inerters, the design aspects and modelling issues are presented in Section 3. Section 4 introduces a novel methodology for generating code-compliant synthetic triplets. Details about the optimization of MFs parameters are provided in Section 5. Section 6, instead, presents the performance of the SMR building protected by single- and multiple-layer MFs through time-history analyses (THAs) in locations with and beyond design seismic conditions. Finally, Section 7 provides conclusions and future perspectives.

2. Description of the superstructure and model reduction

The examined superstructure, the Nuward™ SMR building, incorporates two Generation III + pressurized water reactor (PWR) units, yielding a combined output of 340 MWe (IAEA, 2020). Currently, the SMR is in its early design stage. Fig. 1(b) sketches the available schemes; whilst, Fig. 2 reports the fundamental modes of the SMR FE model. Each PWR unit, with dimensions of approximately 14 m in height and 10 m in diameter, is submerged in water-cooling pools. The walls and slabs of the structure are realized with high-strength reinforced concrete (RC) and with thickness ranging between 0.5 m − 2.5 m (ARIS, 2023). The total weight of the structure is ∼ 200,000 tons. The building was designed considering horizontal peak ground acceleration $PGA_H = 0.3$ g

and vertical $PGA_V = 0.2$ g, according to design basis earthquake (DBE) requirements.

The FE modelling of the SMR building was conducted in the FE software SAP2000 (CSI, 2022). The compact PWRs were treated as solid blocks, firmly connected at the base. The RC components were simulated using quadrilateral shell elements, with reduced RC elastic modulus, to mimic the effects of cracking. The dynamical contributions of the cooling pools were considered by means of simplified models, after Malhotra et al. (2000) and Veletsos & Tang (1986) for the horizontal and vertical direction, respectively. For each pool, the FE is characterised by mass and stiffness values −gathered in Table 1 using point masses and link elements.

The FE model of the structure contains more than 5000 shell and frame elements, with size of stiffness and mass matrices over 30,000x30,000. Whilst refined FE models are essential for accurate internal stress distributions, they become unsuitable for designing and optimizing the seismic protection system. Therefore, to enhance practicality and reduce computational costs, the Craig-Bampton (Craig & Bampton, 1968) component mode synthesis (CMS) technique was applied. The relevant reduced model preserved the modal properties of the superstructure, with a limited numerical burden. In the context of a fixed-interface CMS, the degrees of freedom (DoFs) of the SMR building were categorized into two groups: internal DoFs and boundary DoFs, which represent the DoFs linked to other structures. The system of equations of motion (EoM) of the FE model can be written as:

$$\begin{bmatrix} M_{II} & M_{BI} \\ M_{IB} & M_{BB} \end{bmatrix} \begin{bmatrix} \ddot{u}_I \\ \ddot{u}_B \end{bmatrix} + \begin{bmatrix} K_{II} & K_{BI} \\ K_{IB} & K_{BB} \end{bmatrix} \begin{bmatrix} u_I \\ u_B \end{bmatrix} = \begin{bmatrix} F_I \\ F_B \end{bmatrix} \qquad (1)$$

where subscripts I and B refer to the internal and boundary DoFs, respectively. Due to its thick and densely reinforced structure, the bottom slab of the SMR building was considered as a rigid plate. Consequently, the boundary nodes were defined as the five nodes of the bottom slab, comprising one central node and four corner nodes. As a result, the interactions of both translational and rotational motions with ground − standard solution − or seismic protection systems were assured. The application of the Craig-Bampton transformation matrices, T_{CB}, to (1), provides the reduced model matrices,

$$M_{SMR} = T_{CB}^T M T_{CB} K_{SMR} = T_{CB}^T K T_{CB} \qquad (2)$$

where M_{SMR} and K_{SMR} corresponds to mass and stiffness matrices of the reduced model of the SMR building, respectively. The accuracy of the reduced model was verified with the modal assurance criterion (MAC). In particular, Fig. 3(a) reports the MAC up to the first 200 modes, with values ranging between 0 − no consistent correspondence between the refined and reduced model modes − and 1 − perfect correspondence −.
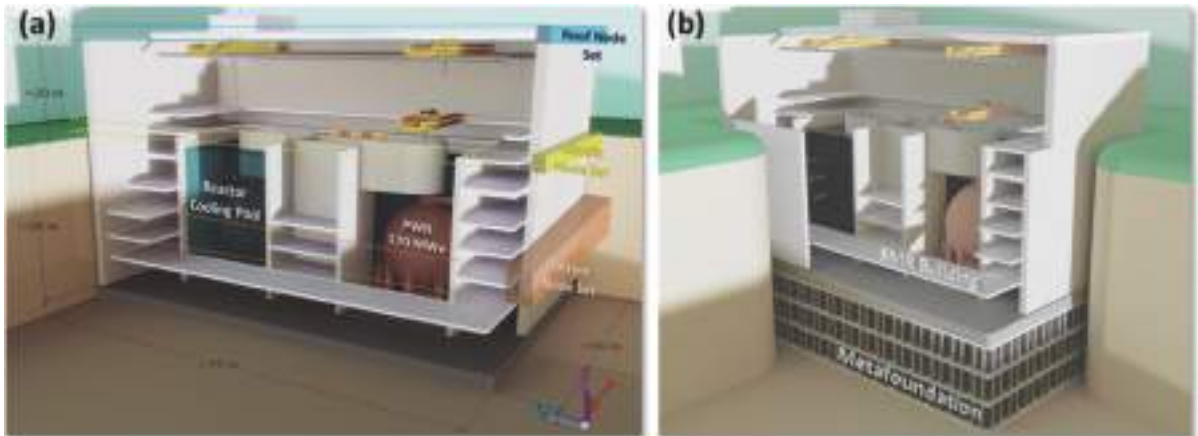

Fig. 1. (a) Schematic of the Nuward™ SMR building; (b) the Nuward™ SMR building with an MF (not in scale).
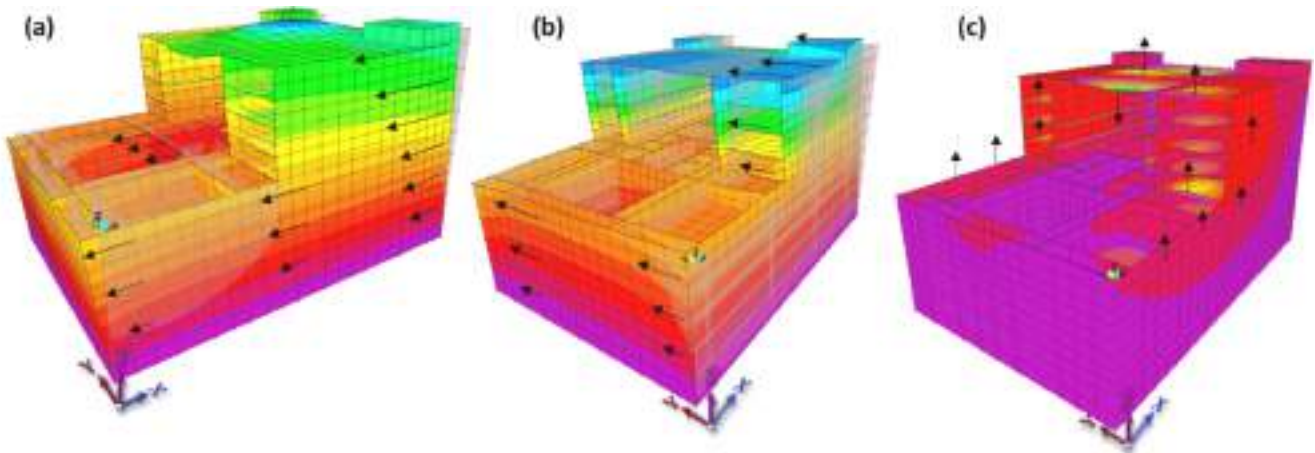
Fig. 2. Fundamental modes provided by FE software: a) X (4.4 Hz), b) Y (3.6 Hz) and c) Z (11.4 Hz) responses.

Table 1
Simplified model masses and stiffnesses of cooling pools.

		Mass (tons)	Stiffness (kN/m)	Frequency (Hz)
Horizontal Impulsive Mass	m_i	8086.9	60.71 e6	13.80
Horizontal Convective Mass	m_c	2097.7	3.67 e3	0.21
Vertical Impulsive Mass	m_{vi}	2710.5	677.62 e6	$\infty(100)$
Vertical Breathing Mass	m_b	7474.1	26.01 e6	9.39

The results confirm that the reduced model consistently mirrors the dynamics of the FE model, except for frequencies below 1 Hz, due to the convective/breathing modes of the pools that account for less than 0.5 % of mass participation (see Fig. 3(c)). These low frequencies are considered negligible and do not impact the results.

In the design and optimization phase, the use of the response spectrum method and frequency domain conversion of the EoMs are required. Thus, the reduced model must satisfy both models' modal orthogonality condition (MOC). However, the Craig-Bampton synthesis does not guarantee the MOC. Consequently, the reduced model must be verified for orthogonality, where mode shapes exhibit no mutual influence in terms of kinetic energy distribution, as depicted in Fig. 3(b). The results show that some high-frequency modes exhibit non-orthogonality; however, mass participation ratios of these modes, Fig. 3(d), show that the participation is negligible, and therefore, those modes do not affect the orthogonality criterion.

To provide a comprehensive overview, the limitations of the reduced model are outlined herein: i) As depicted in Fig. 3, the validity of the reduced model is limited within the frequency range determined by the chosen retained modes; ii) the method's effectiveness depends on the selection of modes and boundary conditions; for instance, the rigid plate assumption may not be adequate for structures with more flexible slabs;
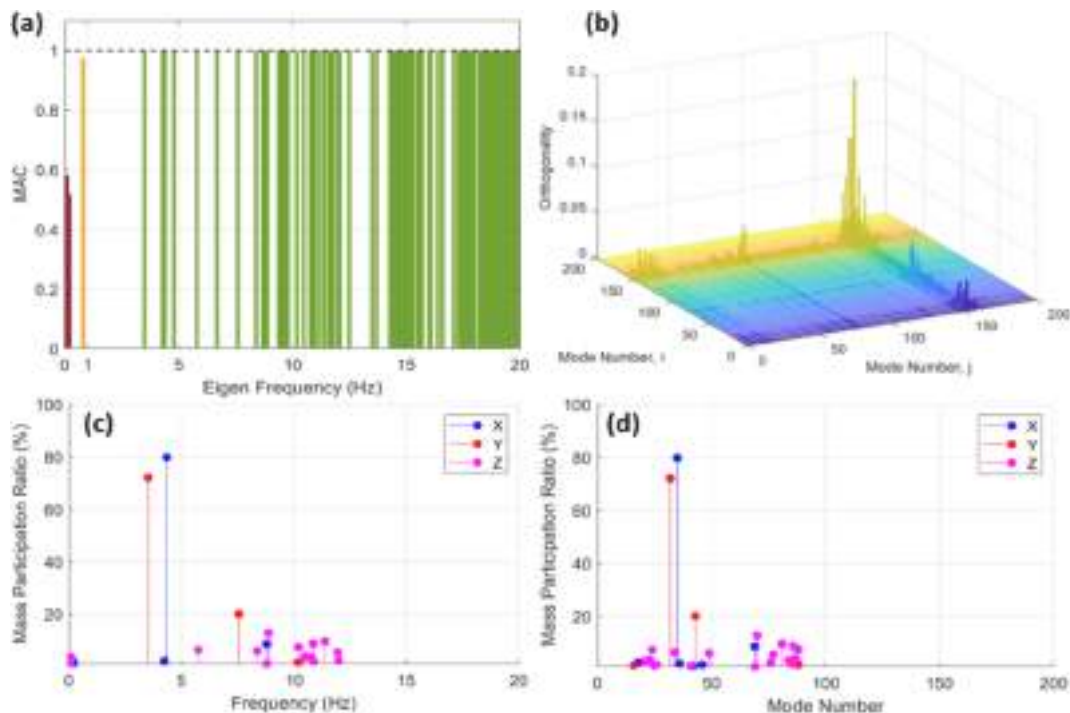

Fig. 3. (a) MAC results for the first 200 modes; (b) the orthogonality conditions, >0 is non-orthogonal; (c) mass participation ratios w.r.t frequency; (d) mass participation ratios w.r.t mode numbers.

iii) the method lacks accuracy when applied to nonlinear or non-proportionally damped systems; and iv) the initial transformation results in high computational costs, especially in systems with complex boundaries, resulting in a relatively large number of DoFs to retain and, thereby, limiting the reduction efficiency.

Due to the dominance of RC elements, a 3 % Rayleigh damping was applied to the structural elements. This ratio is lower than the value provided by the Regulatory Guide 1.61 (U.S. Nuclear Regulatory Commission, 2007), owing to the compactness and stiffness of the structure (U.S. Nuclear Regulatory Commission, 2015). Since the aim of the MF is to prevent any damage to the superstructure, the aforementioned ratio is considered the same for all hazard levels. Accordingly, the damping matrix $\mathbf{C}_{SMR}$ was computed from the reduced mass $\mathbf{M}_{SMR}$ and stiffness $\mathbf{K}_{SMR}$ matrix. Their size amounts to 230x230.

3. Modular unit cells, design procedure and modelling issues of metafoundations

The concept of MFs is inspired by the well-known and widely adopted acoustic metamaterials (Basone et al., 2019). Briefly, metamaterials derive their properties from the relevant structural patterns; therefore, they can be designed to transmit, trap and filter waves. To achieve specific effects on various ranges of waves, these materials are typically created by arranging smaller, ad-hoc designed unit cells in a periodic pattern, as illustrated in Fig. 4(a). A specific class of metamaterials, namely locally resonant metamaterials (LRMs), exploits the concept of resonance at a local scale, as depicted in Fig. 4(b). This permits to absorb or scatter waves at specific frequencies, effectively controlling the propagation of waves. Due to their low-frequency wave attenuation ability, LRMs are especially advantageous in the field of seismic engineering. Along this line, Fig. 4(c) illustrates a periodic and finite 1D LRM that can effectively suppress waves within a tuned frequency region. In periodic lattices, these regions, known as band gaps, are determined analytically by a dispersion analysis, using the Floquet-Bloch theorem. Details are provided in Appendix A for interested readers.

This paper introduces an innovative seismic protection system that replaces the traditional foundation of superstructures with an MF layer. Like metamaterials, MF consists of purposely designed unit cells, emphasizing the benefits of LRMs, as illustrated in Fig. 4(c). By integrating established concepts of seismic isolation and tuned mass dampers (TMDs) into the unit cells, MF offers the following advantages:

- absorption of horizontal and vertical seismic waves through multiple mass dampers (resonators);
- multi-directional flexible interface between the ground and superstructure, that reduces, therefore, the energy transfer to the SMR;
- wave attenuation through local resonances and propagating wave dispersion;
- leveraging the unit cell approach, that offers flexible and adaptable modular seismic protection solutions.

Therefore, the unit cell is the key element of the MFs, whose design is provided in Fig. 5(b). Briefly, it contains two main structures: the main cell and the resonator. The main cell comprises the RC slab and composite columns, resembling a flexible frame. The resonators are realized with RC blocks and connected to the slab with a spring-damper system. Among various options, wire ropes are preferable for their flexibility in both horizontal and vertical directions. Steel and reinforced concrete used in the MF and shown in Fig. 5a minimise the long-lasting problem that could occur with the use of rubber-based materials, e.g. Witarto et al. (2019). The MF unit cell incorporates basic structural elements (columns and slabs), that provide modularity and eliminates the need for complex design procedures. Unlike conventional isolation solutions, the inherent structural redundance of a MF makes it insensitive to vertical load distributions, at the expense of limited extra excavations.

3.1. The role of modular metafoundations in the design standardisation of SMRs

Modularization and design standardisation are key factors in enhancing the viability and attractiveness of SMRs, especially compared to large NPPs (Lloyd et al., 2021). Primarily, standardisation results in the repeated production and construction of similar units, oriented to
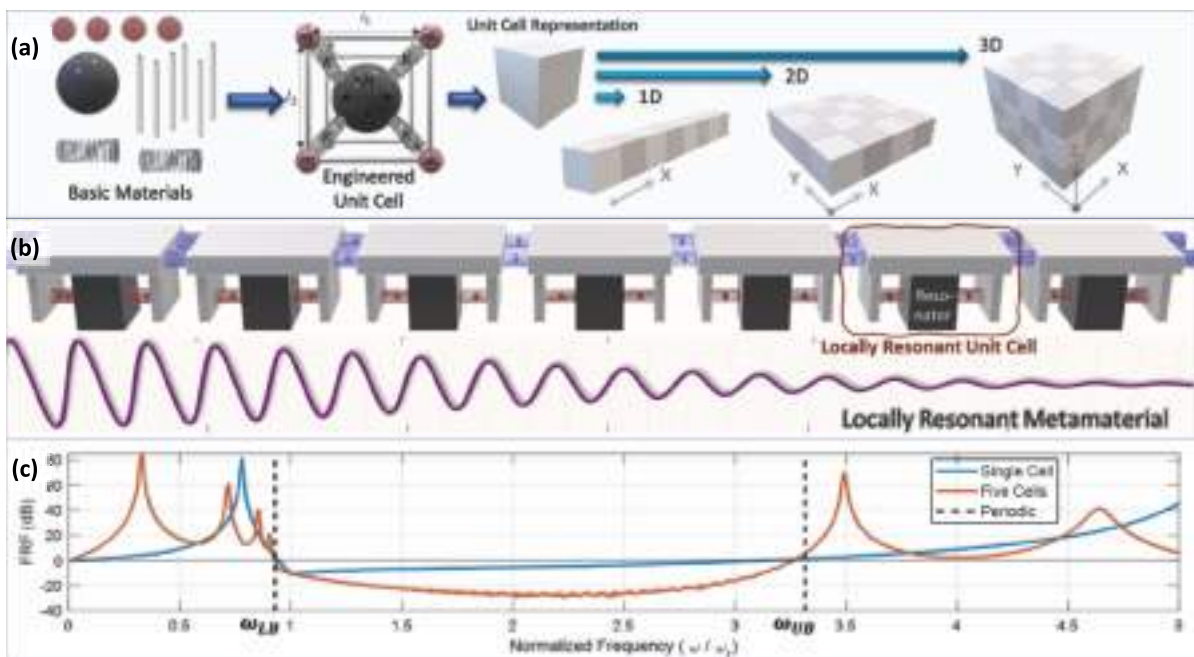

Fig. 4. a) Example of an acoustic metamaterial with various arrangements in 1d, 2d, and 3d, realized with ad hoc designed unit cells; b) 1d lrm and wave attenuation through the lattice material; c) frf of finite locally resonant metamaterials with single and five cells compared to the band gap boundaries of the periodic counterpart discussed in appendix a.
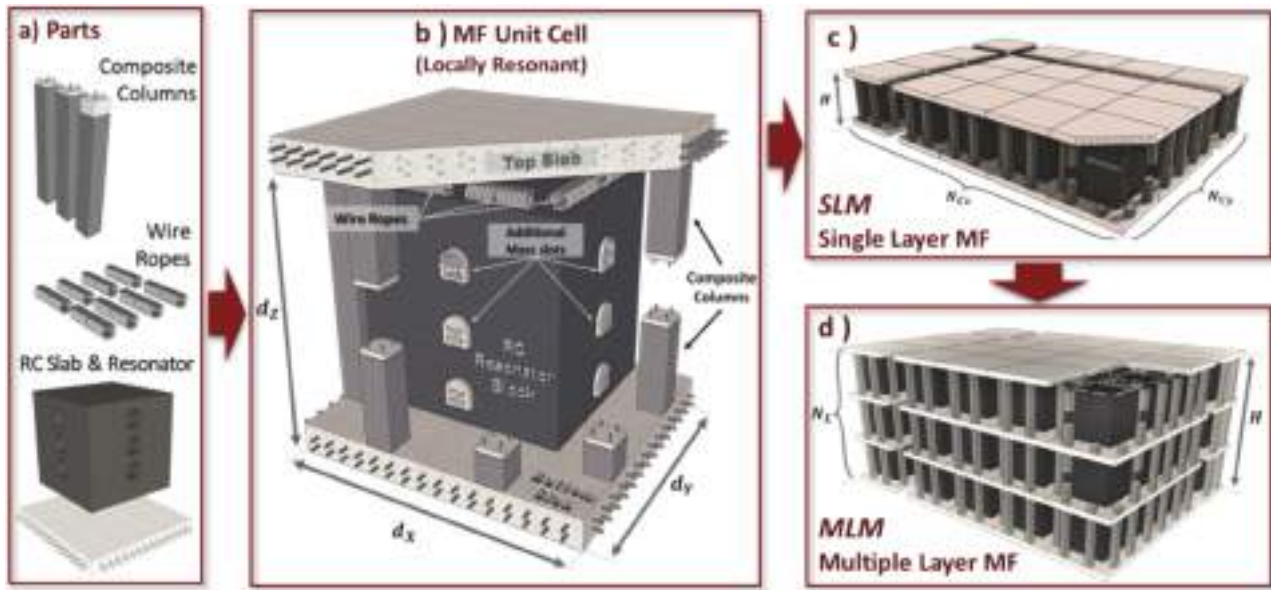
Fig. 5. (a) Basic components of a unit cell; (b) MF unit cell; (c) Single layer MF (SLM); (d) Multiple layer MF (MLM). Dimensions of elements are not in scale.

cost reduction, shortened construction and deployment timelines, as well as improved safety, flexibility, and scalability of design projects.

Along these lines, the proposed MF is conceived to replace and simplify the complex and detailed design procedures of the structural components of the SMRs, including walls, slabs, connections, and more, with a comparatively straightforward design procedure. Moreover, due to its metamaterial nature, the MF entails modularity advantages. In particular, ad-hoc designed LRMs unit cells, see Fig. 5b, can be combined to form a single-layer MF (SLM), as indicated in Fig. 5c. By stacking these layers as depicted in Fig. 5d, a multiple-layer MF (MLM) is created. Thus, the adaptation of specific unit cell designs allows for the MF to be tailored for various hazard conditions and requirements; hence the MF represents a versatile solution for the design standardization of SMRs. MFs also offer design flexibility by fixing parameters as the number of cells in a layer ($N_{C,x}, N_{C,y}$), the height of the layers (d_z), the column section size/type, and the number of layers (N_L).

Moreover, the unit cell structure of the MFs enables adjustments for variations in the superstructure loads and behaviour during a lifetime. For instance, concerning the retuning of resonators, special sockets in the same resonators, see Fig. 5 (a), enable post-construction modification by adding or removing portable masses.

It is worth mentioning that the proposed MFs incorporate conventional structural elements, such as reinforced concrete and steel members; and, in agreement with design standards (ASCE/SEI, 2016), these components are engineered to maintain their elasticity and integrity up to the Design Basis Earthquake levels. In addition, they are not going to experience damage for the beyond DBE of the SMR. Consequently, regular maintenance is not anticipated over the lifespan of the NPP. However, routine inspections and unforeseen events, such as disasters exceeding design levels, may necessitate repairs, most likely involving wire ropes. In such scenarios, the modular system enables unit cell-based interventions, such as wire rope replacement where each resonator can be lowered by comparatively small jacks. Additionally, given that resonators require some distance from the nearest columns, about 0.5 m, natural inspection and maintenance pathways will be readily accessible.

3.2. Design of composite columns and RC slabs

The design of the composite columns of the MFs complies with Eurocodes 1994-1-1 (European Committee for Standardization, 2004a), Eurocodes 1993–1-1 (European Committee for Standardization, 2005b),

whilst for the fire hazard with Eurocode 1994–1-2 (European Committee for Standardization, 2005a). As a result, the composite columns were designed to satisfy the R180 fire-resisting rating. Hollow rectangular steel sections filled with RC were considered for their low shear stiffness and high moment capacity. The NRC 1.60 (USNRC, 2014a) response spectrum was then applied for seismic design. Following Eurocode 1998–1 (European Committee for Standardization, 2004b), the excitation in the orthogonal planar directions X, Y, or Z was reduced to 30 % recursively. The design included all reduced model modes and responses were combined with the complete quadratic combination (CQC) method (Chopra, 2017).

The MFs must comply with the safe shutdown earthquake (SSE) limit state, under which structures must ensure the safe shutdown of the NPP (ASCE/SEI, 2016). It must be noted that this specification disregards the progress in the next-generation SMRs such as passive cooling; subsequently, this limit states might be modified in the future. Elastic behaviour of structures is considered and, therefore, the behaviour-reduction factor is assumed as $q = 1$.

Owing the modularity of the unit cell structure, all columns in the MFs are the same; thus, the column design is governed by the most critical column. It must be also emphasized that the number of columns and their heights, which is equal to the unit cell height d_Z, influence the column section size and effect the stiffness of the MF, thus impacting the performance. Clearly, various sections can satisfy the design requirements. As proven in previous studies (Guner et al., 2022), the minimum stiffness in both horizontal and vertical is preferable. Therefore, a possible section can provide the best flexibility in a specific direction, while resulting in reduced performance for the others. Moreover, the section width plays an important role in the maximum allowable resonator size. In particular, as the size and number of columns are reduced, bigger/heavier resonators can be used. This issue is further explained in Subsection 5.2.

In the case of MLMs, see Fig. 5(c), the rigid behaviour of the main cell slabs must be verified for proper modelling, optimum performance and safety. Although the advantages of slab flexibility and staggered column layout are evident for the vertical direction (Franchini et al., 2020), incorporating non-continuous columns along the layers in NPP seismic design raises complex issues, rendering them unfeasible. Therefore, the slab thickness has been considered to be $t_s = 0.5$ m. The required reinforcement areas and maximum deflection at the centre of a unit cell slab are provided in Fig. 6. In particular, the adopted unit cell dimensions are

$d_x = 7.5m$, $d_y = 8.3m$, and $d_z = 18m$. Under the heavy resonator loads, the slab exhibited less than 1 mm displacement, providing sufficient stiffness for the mechanical model.

3.3. Inerters

For an effective seismic protection, depending on the superstructure size and weight, significant space allocation under the superstructure is required for the MFs. However, this may not always be feasible due to cost and site conditions. Moreover, it is clear that the number of layers N_L can become a design variable (Basone et al., 2019). However, their study showed that fitting multiple layers into a constant MF height, H, entails greater column stiffnesses, thus, resulting in a loss of performance. Therefore, to reduce MF height and/or to compensate for the performance losses due to increased column stiffness, the use of inerters is considered.

An inerter is a linear two-terminal mechanical device, see Fig. 7 (a), that creates a resisting force, F, proportional to the relative acceleration on its terminals (Smith, 2002). It can be considered a counterpart of a classical spring, where forces are generated proportionally to relative accelerations. However, the phase delay of the inerters is π, which indicates that inerters play a role as a negative spring (Chen et al., 2009). Similarly to springs and dampers, inerters are also associated with a constant b, namely the inertance,. The resisting force, F, is a function of inertance and relative acceleration of the two inerter terminals, i.e., $\ddot{u}_1$ and $\ddot{u}_2$, as depicted in Fig. 7(b). Inerters have a mass significantly lower than their inertance b, generally disregarded when performing seismic analyses (Marian & Giaralis, 2014).

For the SMR application, inerters were positioned between the bottom of the resonators and the ground. To the best of the authors' knowledge, there is no triaxial inerter available. Therefore, separate uncoupled inerters were considered for each direction (X, Y, and Z). Moreover, to allocate larger inerters and performing maintenance activities, a total height of 0.75 m for the resonators from the bottom was trimmed. Ma et al., (2021) reported inerters with $b \geq 2000 tons$.
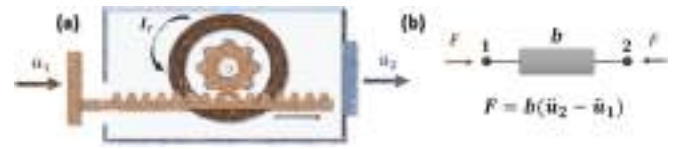

Fig. 7. (a) Model of a rack-pinion inerter; (b) schematic of an inerter with inertance, b.

3.4. Modelling of metafoundation

The MFs were modelled and analysed in 3D. As a result, the seismic protection capacities of the MFs were also investigated for rocking and torsional responses of the superstructure. Specifically, to reduce the computation time of design, optimization and analysis, a simplified MFs modelling methodology is proposed. The continuous/discrete modelling approach is sketched in Fig. 8.

The numerical modelling of the MFs is based on three main assumptions: a) the numerical modelling of the MF layers aligns with the reduced SMR model, thus maintaining stability with 5 boundary DoFs for a proper translational-rotational transfer. Each layer's slab is modelled using five key nodes—four corners and one centre. As each layer has multiple unit cells with columns and resonators, rigid links between the MF and the superstructure were considered (see Fig. 8 and Cook et al., 2007). Hence, matrices were derived based on the relative locations of each column and resonator connection to the designated node.

b) The column masses were condensed into the slab masses; whilst, the columns stiffnesses were modelled according to the Timoshenko formulation. c) Owing to the symmetric arrangement of wire ropes, each resonator was considered with a single node at its centre of gravity with three translational DoFs, i.e., without the rotational DoFs. Nonetheless, the contribution of the resonators to the rotational DoFs of the complete MF and superstructure was assured and computed by means of the rigid link transformation matrix **Q**. The coupled mass and stiffness matrices of the controlled superstructure were assembled as follows:

$$M_C = \begin{bmatrix} M_{SMR,II} & M_{SMR,BI} & 0 & 0 \\ M_{SMR,IB} & M_{SMR,BB}+M_{MF,1} & 0 & 0 \\ 0 & 0 & M_{MF,2...n_L}+M_{B,(3n_R+1...3n_Rn_L)} & -M_{B,(3n_R+1...3n_Rn_L)} \\ 0 & 0 & -M_{B,(3n_R+1...3n_Rn_L)} & M_R+M_B \end{bmatrix} \tag{3}$$

$$K_C = \begin{bmatrix} K_{SMR,II} & K_{SMR,BI} & 0 & 0 \\ K_{SMR,IB} & K_{SMR,BB}+K_{M,1}+Q_1K_{R,1}Q_1^T & K_{M,12} & -Q_1K_{R,1} \\ 0 & K_{M,21} & K_{M,2...n}+Q_{2...n}K_{R,2...n}Q_{2...n}^T & -Q_{2...n}K_{R,2...n} \\ 0 & -K_{R,1}Q_1^T & -K_{R,2...n}Q_{2...n}^T & K_R \end{bmatrix} \tag{4}$$
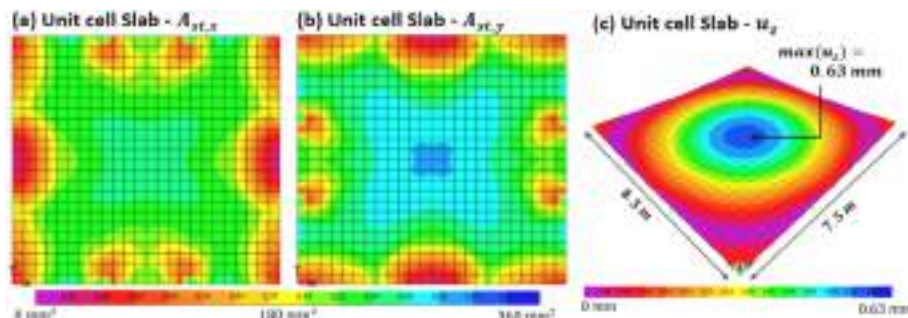

Fig. 6. Unit cell slab details: required reinforcement area for (a) X-direction; (b) Y-direction; and (c) vertical displacements.
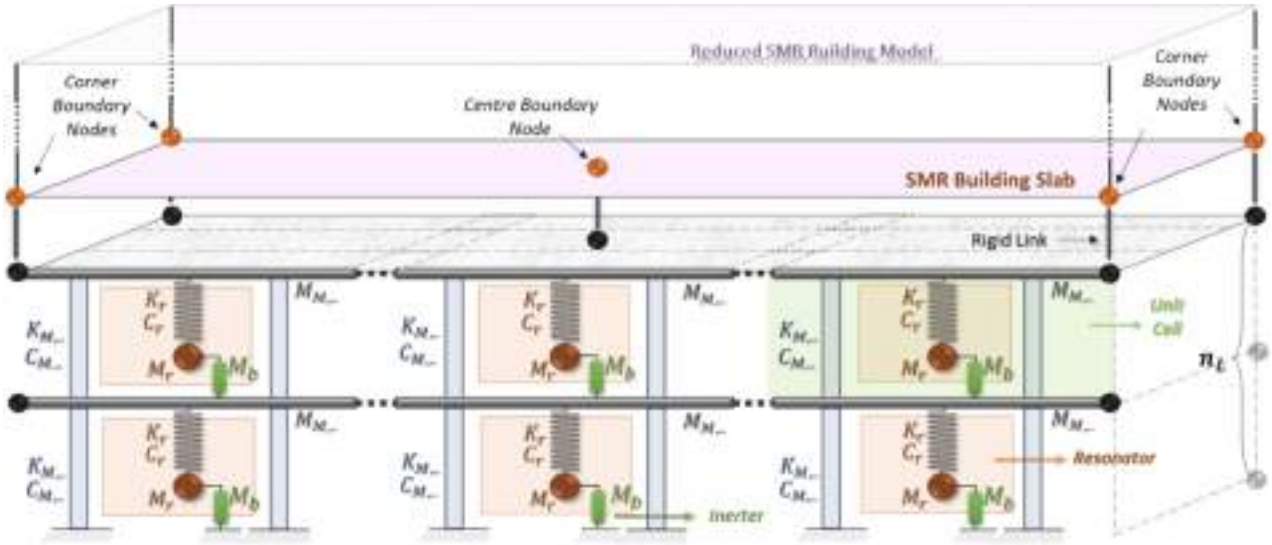
Fig. 8. Discrete MF-Reduced SMR building coupled model spring-mass representation for triple layers with inerters.

where subscripts M, R, n_L represents the main cell, resonator and number of layers, respectively. Subscript C represents the controlled structure. $\mathbf{M_B} = diag(+b, \cdots, +b)$ represents the additional mass terms resulting from the inerters; $b = 0$ corresponded to the case of no inerter. The damping matrix $\mathbf{C_C}$ had the same structure as Eq. (4). The resonator stiffness and damping matrices, $\mathbf{K_R}$ and $\mathbf{C_R}$ were computed as follows:

$$
\mathbf{K_R} = \begin{bmatrix} \omega_{r,x}^2 m_r & & & 0 \\ & \omega_{r,y}^2 m_r & & 0 \\ 0 & & \omega_{r,z}^2 m_r & \\ & 0 & & \ddots \end{bmatrix}_{(n_L n_R)^2} \mathbf{C_R}
$$

$$
= \begin{bmatrix} 2\zeta_{r,x}\sqrt{k_{r,x}m_r} & & & 0 \\ & 2\zeta_{r,y}\sqrt{k_{r,y}m_r} & & 0 \\ 0 & & 2\zeta_{r,z}\sqrt{k_{r,z}m_r} & \\ & 0 & & \ddots \end{bmatrix}_{(n_L n_R)^2} \quad (5)
$$

where m_r, ω_r and ζ_r corresponds to the mass, frequency and damping ratio of the resonators; whilst subscripts x, y and z indicate directions.

4. Ground motion model for code compliant seismic triplets

4.1. Code requirements

To accurately model the coupled dynamical behaviour of the NPPs, current codes and standards, e.g., the USNRC SRP 3.7.1 (U.S. Nuclear Regulatory Commission, 2014b) and the CSA N289.3 (CSA, 2010), impose the following requirements for triplets selection.

  (i) Compatibility of the time series $A(t)_{H1}, A(t)_{H2},$ and $A(t)_V$ with the target ground response spectra S_{H1}^T, S_{H2}^T and S_V^T, respectively. Generally, it holds true $S_{H1}^T = S_{H2}^T = S_H^T$, and, if not specified, $S_V^T = 2/3 S_H^T$ is applied to the frequency range of interest.
  (ii) Statistical independence between each pair of time histories. This is considered satisfied if the absolute value of the correlation coefficient does not exceed 0.16 (U.S. Nuclear Regulatory Commission, 2014b) or 0.30 (CSA, 2010).
  (iii) The strong motion duration evaluated by the time for the Arias Intensity I_a has to rise from 5 % to 75 % (U.S. Nuclear Regulatory Commission, 2014b) or to 95 % (CSA, 2010) uniformly with time.
  (iv) Lastly, the time histories result in no displacement's baseline drift. Since code-compliant natural recorded triplets are scarcely available, the GMM was deployed to generate horizontal and vertical ensembles of synthetic time histories, from which to extract code-compliant synthetic triplets. Further details on the calibration and set up of the GMM are provided in Appendix B.

4.2. Procedure for generating triplets of synthetic time histories

To generate triplets, i.e. 3 component direction time histories, spectral compatible and statistically independent, the flowchart depicted in Fig. 9 has been followed. Specifically, from the generated horizontal GMs a first horizontal-time history $A(t)_{H1}$ is extracted. According to maximum spectral acceleration at a given period $S_a(T_x)$ or maximum PSD, in the given range, compatibility of the generated GM is checked. In particular, the compatibility is verified regarding the target response spectra and the time histories code requirement points (iii) and (iv) (i.e., no baseline drift and smoothness of the increase of the Arias intensity measure) as stated in Subsection 4.1.

Next, the second horizontal component is extracted by the generated horizontal GMs. Again, compatibility is checked on the seismic record selected on the $S_a(T_x)$ or PSD criteria. To check the statistical independence of the two seismic records, the Hilbert-Schmidt Independence Criterion (HSIC) implemented by Chwialkowski and Gretton (2014) is deployed. The test procedure is based on computing the Hilbert-Schmidt norm of a cross-spectral density operator (Fourier transform of the covariance operator at each time lag). The resulting statistic is a function of frequency and must be zero at all frequencies for independence. The test satisfies two properties: it is consistent against any fixed alternatives, and it is non-parametric. This translates into neither *a priori* assignment of a particular structure for dependence (such as linear correlation), nor parametric model identification of the time series.

Finally, the vertical component is extracted by the ensemble of the GMM_V. In agreement with Bozorgnia and Campbell (2016), the V/H ratio was adopted to select a vertical GM. Specifically, the acceleration spectra of the vertical GM must be compatible with the ratio of the horizontal spectrum in the period range of interest. The V/H ratio is commonly used to develop a vertical design spectrum by using it to scale the horizontal design spectrum from seismological parameters of scenario earthquakes (Gülerce and Abrahamson, 2011, Bommer et al.,
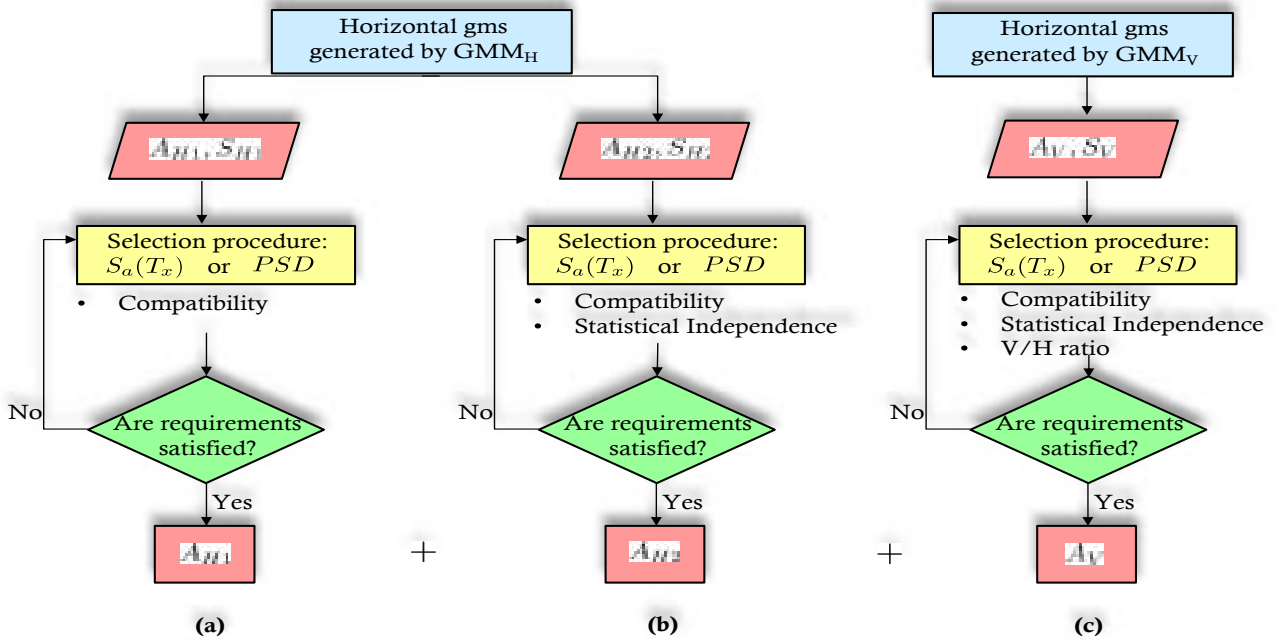
Fig. 9. Procedure for generating triplets of time histories: (a) the first horizontal acceleration time history; (b) the second horizontal time history; (c) the vertical time history.

2011, Akkar et al., 2014). Moreover, the selected vertical component must satisfy the compatibility and statistical independence requirements. Once all the requirements for the 3 components GMs are satisfied, a triplet is defined. The procedure was then repeated to generate 1500 triplets.

4.3. Design and beyond-design synthetic triplet

Aligned with the research objectives, i.e. to support the SMR design standardisation, the SMR building which has been designed for DBE seismic hazard level, has been assumed to be constructed in locations with beyond design basis earthquake (bDBE) hazard conditions. As a result, from the pool of 1500 triplets, first, a set of 100 unscaled triplets was selected for DBE; a second set was selected and scaled for bDBE location with $PGA_H = 0.35g$ (bDBE-1); and lastly, a third set was selected and scaled for bDBE location with $PGA_H = 0.4g$ (bDBE-2). In accordance with the code, the condition $PGA_V = PGA_H*2/3$ was considered. For selection, the following optimization problem, which was solved by a genetic algorithm, was considered. The optimization parameters included: (i) the indices of the selected 100 triplets, and (ii) a constant scaling factor that was applied to all selected triplets (only for

bDBEs). The objective function aimed to minimize the sum of the root-mean-squared (RMS) error above 0.5 Hz and up to 10 Hz between the median of selected triplets and the target spectra for all directions. To prevent under-fitting, negative errors were penalized ten times more than positive values. Consequently, 100 triplets were chosen for each hazard level, and the median of the selected triplets, along with the corresponding target spectra, are illustrated in Fig. 10. Compatibility has been mainly fulfilled in the short period range, i.e., the domain of interest for the SMR application.

For optimization of the resonator parameters, the power spectral density (PSD) function of the input has been determined. Accordingly, an estimate of the mean stationary PSD of the accelerograms, $\overline{S}_{\ddot{u}_g.st}$ was computed as:

$$\overline{S}_{\ddot{u}_g.st}(f) = \frac{1}{NM} \sum_{i=1}^{N} \left| \sum_{j=1}^{M} \ddot{u}_{g.st}^{(i)}(t_j) e^{-j2\pi f t_j} \right|^2 \tag{6}$$

where N and M are the number of accelerograms and the number of time steps in the i-th accelerogram.
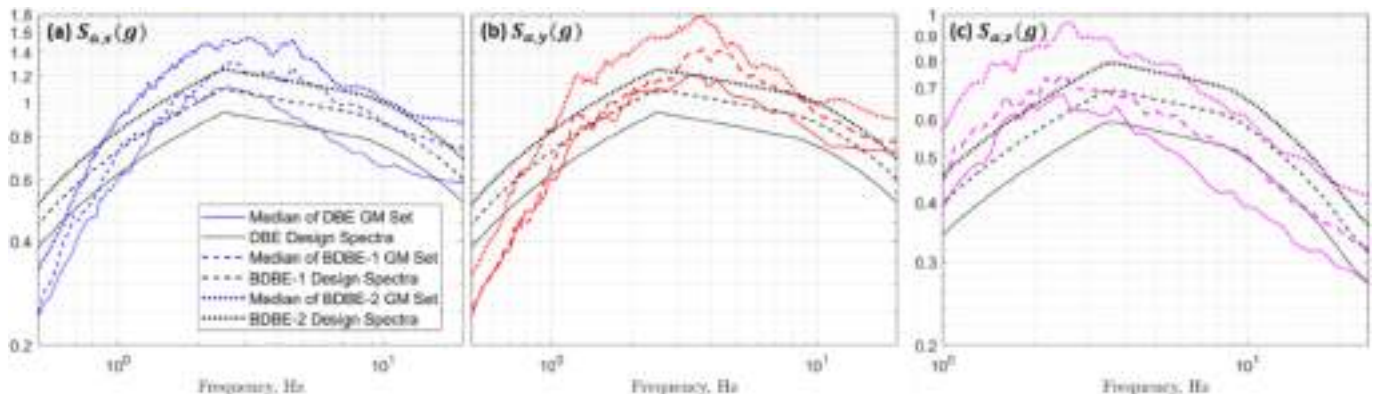

Fig. 10. The median of selected triplets for DBE, bDBE-1, and bDBE-2 hazard levels and corresponding design spectra.

5. Metafoundation parameters and optimisation

To leverage the optimisation process, the optimisable parameters of the MFs include the number of cells in each layer (N_C), the number of layers (N_l), and the unit cell height (d_z), which is equivalent to the height (H) for SLMs, and resonator stiffness/damping values.

5.1. Optimisation of resonators

As highlighted in Fig. 5(a), the resonators were attached to the slab by means of wire ropes. In detail, wire ropes can exhibit high damping ($\zeta_{eq} \approx 0.15 - 0.25$) as reported by Alessandri et al. (2015), which makes them a suitable choice. Here, it must be emphasised that the stiffness determines the attenuation rate and range. Thus, this value must be carefully chosen, considering the feedback of the coupled system and the frequency content of the GMs. Moreover, wire ropes exhibit non-linear behaviour. However, Bursi et. al. (2021) showed that the dynamics of wire ropes can be approximated with equivalent linear spring-damper parameters for specific hazard conditions. Alternatively, wire ropes can be selected to operate in the linear regime. Consequently, the determination of optimized linear resonator parameters, ω_r and ζ_r, deemed sufficient for our research purposes.

Accordingly, the resonator parameters ω_r and ζ_r can be optimized with respect to the frequency response of the coupled MF-SMR system subjected to the seismic input computed through Eq. (7). The optimization was carried out by assembling the system of linear EoMs subjected to GMs:

$$\boldsymbol{M_{SMR}}\ddot{u}(t) + \boldsymbol{C_{SMR}}\dot{u}(t) + \boldsymbol{K_{SMR}}u(t) = -\tau \boldsymbol{M_{SMR}}\ddot{u}_g(t) \tag{7}$$

where $\mathbf{M_{SMR}}$, $\mathbf{K_{SMR}}$ and $\mathbf{C_{SMR}}$ represent the mass, stiffness and damping matrices of the reduced SMR model and τ the influence vector of the seismic input. Replacing $u(t) = u(\omega) \bullet e^{i\omega t}$, the displacement and absolute acceleration transfer function for the SMR, $\mathbf{H_{SMR,d}}$ and $\mathbf{H_{SMR,a}}$ reads

$$\boldsymbol{H_{SMR,d}} = \frac{u(\omega)}{u_g(\omega)} = (-\tau \boldsymbol{M_{SMR}}) \cdot (\boldsymbol{D_{SMR}})^{-1} \quad \boldsymbol{H_{SMR,a}} = \frac{\ddot{u}(\omega)}{\ddot{u}_g(\omega)} = \tau - \omega^2 \cdot \boldsymbol{H_{SMR,d}}$$

where

$$\boldsymbol{D_{SMR}} = (-\omega^2 \boldsymbol{M_{SMR}} + i\omega \boldsymbol{C_{SMR}} + \boldsymbol{K_{SMR}}) \tag{8}$$

The transfer function of the coupled MF-SMR system, i.e. the controlled structure $\mathbf{H_{C,a}}$ follows:

$$\boldsymbol{H_{C,a}} = \tau - \omega^2 \cdot \boldsymbol{H_{C,d}} = \tau - \omega^2 \cdot (-\tau \boldsymbol{M_C}) \cdot (\boldsymbol{D_C})^{-1} \tag{9}$$

The coupled system matrix $\mathbf{D_C}$ can then be obtained by considering coupled system matrices in (8). The PSD of the coupled soil-structure system can be computed for the i-th DoF as:

$$S_{SMR,i}(\omega) = |\boldsymbol{H_{SMR}}|^2 \cdot S_{\ddot{u}_g}(\omega) \quad S_{C,i}(\omega) = |\boldsymbol{H_C}|^2 \cdot S_{\ddot{u}_g}(\omega) \tag{10}$$

where $S_{\ddot{u}_g}(\omega)$ is the input PSD function.

The objective of the optimization problem is selected as:

$$min\left(PI = \sum \left(\|S_{C,i}\|_\infty \Big/ \|S_{SMR,i}\|_\infty\right)\right) \tag{11}$$

which corresponds to the minimization of the peak response of the controlled structure with respect to (w.r.t.) the uncontrolled cases, i.e., rigid foundation (H_∞ optimization). The PI corresponds to the Performance Index and the sum of translational DoFs belonging to boundary nodes, i.e., 5 nodes x 3 DoFs = 15, was considered for the optimization. Accordingly, the variables of the optimization problem can be defined for the 3-DoF formulation of linear resonators as follows:

$$\chi = \{\omega_{r,x}, \omega_{r,y}, \omega_{r,z}, \xi_{r,x}, \xi_{r,y}, \xi_{r,z}\} \tag{12}$$

The presented optimization problem was solved by means of a deterministic optimization algorithm, as in Guner et al. (2022). In the context of column design, several solutions are available. Nonetheless, the design process necessitates prior knowledge of the resonator frequencies; therefore, following the initial design, it is necessary to identify the optimized resonator frequencies, leading to an iterative design procedure, until convergence between initial and optimized resonator frequency values is achieved.

5.2. Selecting unit cell parameters

This study introduces an optimization strategy aimed at determining the optimal dimensions of the unit cells of the MF, illustrated in Fig. 5b. It is essential to emphasize that the optimal dimensions depend on various factors, including the characteristics of the superstructure and site-specific properties such as soil type and seismic conditions. Herein, the objective is to maximize the performance of the modular MFs to achieve an enhanced seismic protection of the Nuward™ SMR building.

With regard to the height d_z, a previous research has demonstrated that increasing d_z in all directions enhances flexibility and, hence, performance (Guner et al., 2022). While this adaptability makes the MF versatile, the total height H of the MF is often constrained by cost and the available space for excavation beneath the structure. It is clear that as the H increases, deeper excavation is required, together with the increased size of structural parts and resonators, resulting in higher costs, logistic problems, and a higher chance of depth-related geological problems. As a result, the selection of H may be limited by various factors. One approach is to consider both the performance and cost of the MF together, as derived by Guner et al. (2022), in which the cost–performance creates a set of Pareto optimal solutions, and the optimum H can be selected by the decision-maker considering the available budget or other factors. The approach considered in this study consists of the selection of H by considering the minimum height that satisfies a required performance target. As mentioned in Subsection 3.1, the design standardization aspect of SMRs is of paramount importance; thus, the performance target can be set to reduce responses in the SMR building to beyond design levels, such that no or minimal modifications will be required.

With regard to the unit cell widths, $d_x \& d_y$, it is clear that due to the footprint of the superstructure on the horizontal plane, d_x and d_y determine the number of unit cells in X ($N_{C,x}$) and Y ($N_{C,y}$) directions. The number of unit cells in a layer, i.e., $N_C = N_{C,x} \times N_{C,y}$, is clearly influenced by the layer stiffness of the MF. It is important to emphasize that each MF, characterized by a set of parameters $N_{C,x}$ and $N_{C,y}$, is associated with a set of suitable column sections, each with varying widths (w_x, w_y) and thickness. To facilitate a comparison, the normalized $S_{C,dir}$ parameter [0,1], see (11), was considered for each direction ($dir = \{x, y, z\}$) in the boundary nodes.

To explore the influence of N_C on the stiffness, SLMs with fixed $H = 12m$, and several combinations of $N_{C,x}$ and $N_{C,y}$ ranging between 7–20 and 5–15, respectively, were considered. The results expressed in terms of $S_{C,dir}$ are provided in Fig. 11. The small dots represent the possible section designs of N_C; whilst big dots represent the minimum possible section design. It clearly emerges that as N_C increases, the minimum horizontal and vertical responses do not consistently exhibit a direct correlation. Specifically, as $S_{C,x} \& S_{C,y}$ values exhibit a decreasing trend, the vertical component i.e. $S_{C,z}$, increases. Therefore, a multi-objective trade-off optimization problem, i.e., a Pareto optimization problem, arises. This can be observed in Fig. 12(a), where the results for $S_{C,x}$, $S_{C,y}$, and $S_{C,z}$ are gathered, and the Pareto points are indicated with black rectangles.

The performance of MFs is also influenced by the resonator masses. Consequently, the optimal selection of $N_{C,x}$, $N_{C,y}$, and column section size should also seek to fit the largest resonator in a unit cell. To render the resonator mass dimensionless, it is normalized by the superstructure
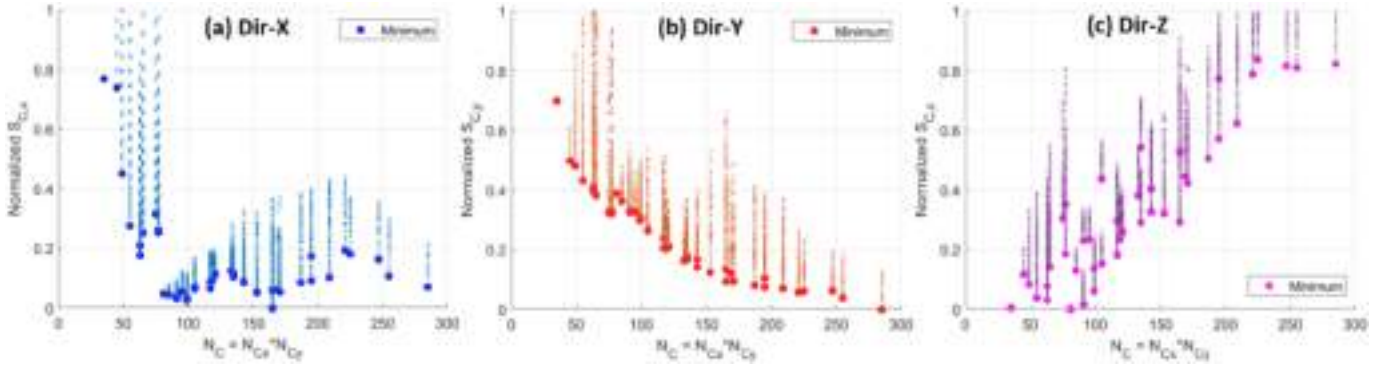
Fig. 11. Variation of the normalized $S_{C,dir}$ w.r.t. the number of cells N_C: (a) direction $-X$; (b) direction $-Y$; and (c) direction $-Z$. The results are scaled between 0 and 1 according to the min. and max. observed values, respectively.
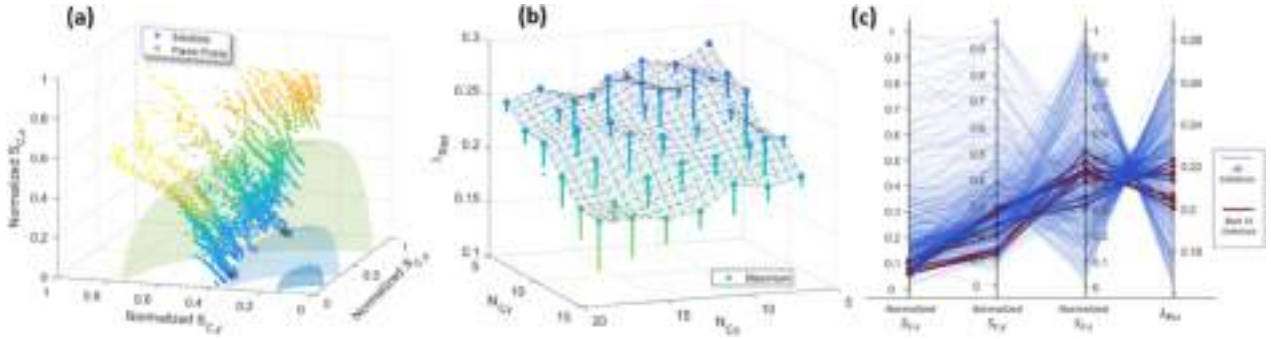

Fig. 12. (a) $S_{C,X}, S_{C,Y}$ and $S_{C,Z}$ results for various N_C values; (b) the influence of N_C on the effective resonator mass ratio λ_{eff}; (c) The parallel plot for various N_C values and the best 10 solutions that minimize $S_{C,dir}$ and maximize λ_{eff}.

weight and expressed as follows:

$$\lambda_{eff} = \sum (m_r + b) \Big/ \sum \boldsymbol{M_{SMR}} \tag{13}$$

where m_r represents the single resonator mass, b is the inertance and λ_{eff} is the effective resonator mass ratio. The λ_{eff} for available designs for various $N_{C,x}, N_{C,y}$ and $b = 0$ are presented in Fig. 12(b). It is clear that as N_C increases, less volume becomes available to the resonators and λ_{eff} decreases. The increase of resonator mass between $N_C = 81$ $(\lambda_{eff} = 0.27)$ and $N_C = 285$ $(\lambda_{eff} = 0.17)$ is approximately 63 %; this result clearly highlights the importance of λ_{eff} on the optimal solution.

Hence, to select an optimal solution, the values $S_{C,x}$, $S_{C,y}$, $S_{C,z}$, and $-\lambda_{eff}$ should be minimized. Given the 4-dimension, the outcomes can be represented using a parallel plot, as depicted in Fig. 12(c). The Pareto front can be computed by taking the closest points to the Utopian point, i.e. the point where all objectives reach their optimum values. The Pareto front with the best 10 solutions that minimize $S_{C,dir}$ and maximize λ_{eff} are showcased in Fig. 12(c).

6. Time history analyses and design standardisation

6.1. Performance of single layer metafoundations

Both modelling and analyses of the SMR-MF were conducted in MATLAB (MathWorks, 2022). The time history analyses (THAs) were performed through Newmark's integration scheme with a constant average acceleration (Newmark, 1959). The results from the reduced model were converted to responses of the full FE model by using (pre-multiplying) the Craig-Bampton transformation matrix, T_{CB} adopted in (2).

Given that the SMR building is represented by a complex FE model, to capture the overall behaviour of the building, three sets of nodes, see

Fig. 1(b), at different z levels were selected: (i) nodes at the level of the reactors and pools, $-18m < z < -10m$, namely set of bottom nodes; (ii) nodes at $z \cong 0m$ or ground level, middle nodes set; and (iii) nodes at the roof level, $z \cong 20m$. After gathering the translational acceleration history of each node in these three sets, each history was subjected to the Fast Fourier Transform (FFT), and frequency contents were obtained. For each set, finally, the average frequency content of all nodes in the set was computed.

To establish reference response values and set a performance target for standardisation, the SMR building with a rigid foundation underwent analyses using the DBE triplets established in Section 4. The average FFT results for each set, corresponding to the rows, are presented in Fig. 13, showing the median values of 100 GMs with shades representing percentiles between 5–95 %. Rows depict the averages of node responses from the roof, middle, and bottom node sets, respectively. Each column in the Figure instead, from left to right, corresponds to the X, Y, and Z directions. The blue and red colours denote horizontal directions (X and Y), whilst the vertical direction (Z) is represented in magenta; these attributes are consistent throughout the paper.

The response is predominant around 3–10 Hz in the X and Y directions, whilst in the vertical direction, peaks are observed beyond 8 Hz, although these responses are smaller than the horizontal ones. It is evident that the responses between directions are strongly coupled. When examining the results across different sets, it becomes evident that the outcomes from the middle node set sufficiently represent the overall structural response with negligible error. Therefore, throughout the paper, the results from the middle node-set are utilized for a more straightforward presentation.

The FFT amplitude is shown in Fig. 14(a) for the SMR building with a fixed base, and for two coupled SMR-MF systems subjected to triplets of DBE, bDBE-1 ($PGA_H = 0.35g$ or 117 % of DBE), and bDBE-2 ($PGA_H = 0.4g$ or 133 % of DBE), respectively. The considered MFs
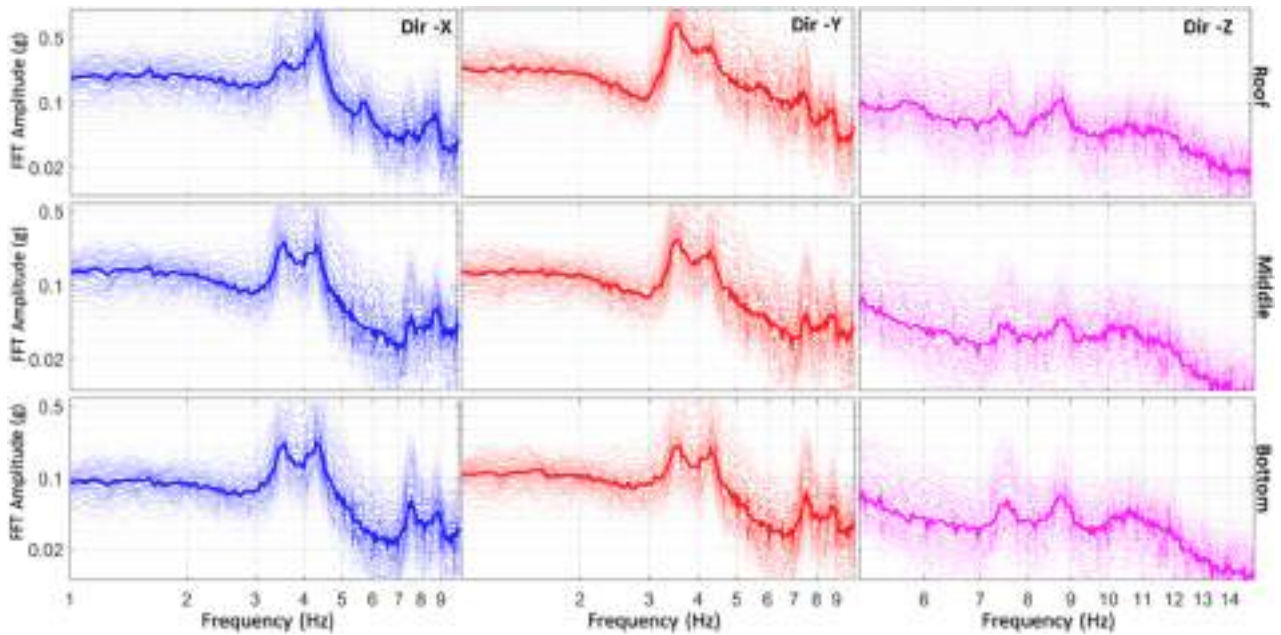
Fig. 13. The median FFT amplitude results for the SMR building exposed to DBE-level triplets are illustrated. The shades indicate the percentiles ranging from 5 % to 95 %. The columns, from left to right, display results for the X, Y, and Z directions, respectively. Rows depict the averages of node responses from the roof, middle, and bottom node sets, respectively.
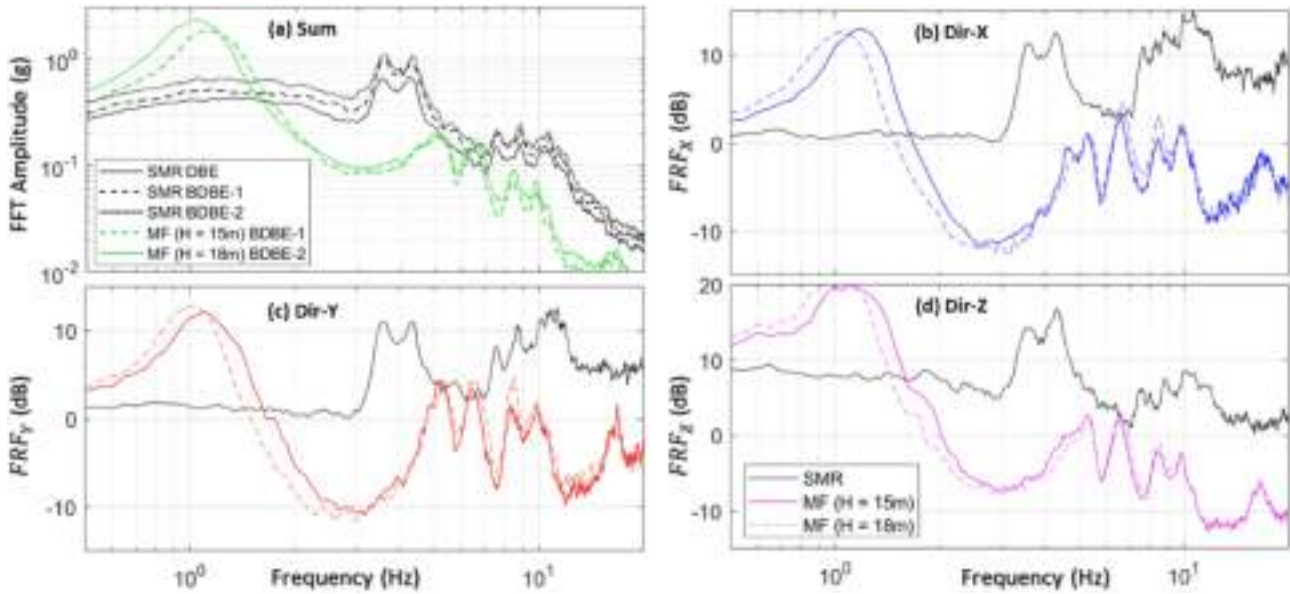

Fig. 14. (a) Averaged FFT amplitude and (b-d) FRF results for the middle node set of the SMR building and SMR-MF coupled systems subjected to bDBE-1 & bDBE-2 triplets. Black lines represent the SMR performances with fixed bases, whilst coloured represent the SMR equipped with MF with different heights, H.

Table 2
Optimal parameter values for bDBE-1 and bDBE-2 designs.

PGA	N_L	d_z	$N_{C.x}$	$N_{C.y}$	Col.w_x	Col.w_y	Col. t	$\omega_{r.x}$	$\omega_{r.y}$	$\omega_{r.z}$	$\xi_{r.x}$	$\xi_{r.y}$	$\xi_{r.z}$	b
(g)		(m)			(m)	(m)	(m)	(rad/s)	(rad/s)	(rad/s)	(%)	(%)	(%)	tons
0.35	1	15	7	9	1.24	1.44	0.035	17	15	23	20	20	16	0
0.4	1	18	9	9	1.26	1.48	0.035	14	16	23	20	20	17	0

have heights ($N_L = 1, H = d_z$) of 15 m and 18 m for bDBE-1 and bDBE-2, as summarized in Table 2. The H of the considered MFs were chosen to match the performance criteria as derived by Guner et al. (2022).

Due to strong coupling effects between translational motions, the combination of FFT amplitudes of −X, −Y, and −Z translational directions at the middle node-set are displayed. It is evident that increased PGA values lead to a significant increase in structural responses, preventing the use of standard SMR building design in beyond-design

locations. Conversely, the SMR building protected by MFs shows notably reduced acceleration responses above 2 Hz. However, due to the introduced flexibility, MFs transfer energy to the lower frequencies, i.e. below 2 Hz, resulting in increased peak low-frequency responses. Although this may necessitate redesign and specific protection for low-frequency equipment, the SMR building mass participation is above the 3 Hz range, therefore satisfying the standardization target.

To delve deeper into the impact of MFs, the frequency response function (FRF) of the middle node set of the building is computed for each direction and depicted in Fig. 14(b-d). The results support earlier findings. In the horizontal direction, a clear attenuation is observed above 1.65 Hz and 1.5 Hz for H = 15 m and H = 18 m MFs, respectively. Notably, an increased response is noted at the 5–6 Hz range in the −Y direction, indicating limitations in the resonator's attenuation frequency range. In the vertical direction instead, a solid and apparent attenuation is evident above 7 Hz, confirming the effectiveness of the MFs against vertical actions.

6.2. Single layer metafoundation with inerters

As anticipated in Subsection 3.3, inerters decrease the size of the resonators and entail a possible reduction of the height of the MFs. However, as derived in Subsection 3.6, the reduction of the MF height increases column stiffnesses, resulting in a performance drop. To investigate this matter, SLMs with no inerter ($H = 18m$, $\lambda_{eff} = 0.36$) and with inerter ($H = 9m$, $\lambda_{eff} = 2$) were analysed using the bDBE-2 triplets. The average FFT results for the middle sets are presented in Fig. 15(a), and the relevant FRFs are in Fig. 15(b-d). It is evident that the MF with inerters performs equivalently within an acceptable performance above 2.7 Hz compared to the $H = 18m$ MF. Nevertheless, in the lower frequency range where resonator effects are limited, there is a significant performance loss. A major drawback is that owing to increased stiffness, attenuation begins at 2.7 Hz, whereas with $H = 18m$, attenuation starts at 1.5 Hz. This limitation restricts the use of the reduced MF with inerters together with flexible structures and components.

6.3. Multi-layer metafoundations

As highlighted in Section 3, the MFs are grounded in the concept of metamaterials, specifically, locally resonant metamaterials deepened in Appendix A. However, the presented SLMs exhibit limited benefits due to finite periodicity. To achieve proper attenuation improvement, using multiple layers is necessary for MFs; nevertheless, a notable drawback emerges from the constrained space beneath the superstructure. The restricted available space necessitates reducing layer heights when increasing the N_L, leading to notably stiffer layers. Assuming a constant overall MF height, although acceptable performance can be achieved with $N_L = 1$, the SLM demands the manufacturing and installation of large resonator blocks, as seen in the $H = 18m$ SLM. Additionally, the provided FRF results in Fig. 14(c) indicated that SLMs prove effective in a narrow frequency range. In particular, see Fig. 16, the SLM with $d_Z = 18m$ is compared with the MLMs with $N_L = 2 - d_Z = 9m$ and $N_L = 3 - d_Z = 6m$. The total height of MFs is the same, $H = 18m$, and THAs are conducted considering bDBE-2 triplets. From the FFT amplitude results, a careful reader can observe that the SLM perform better than the MLMs above 3 Hz, i.e. a 4–5 Hz region, where the response exceeds the SMR at the DBE. However, one significant improvement can be seen in the peak responses below 3 Hz, where MLMs reach lower peak values compared to the SLM. This can also be seen in FRF results.

To overcome the reduced performance of MLMs, inerters can be used between resonators and the underlying layer slabs (ground for the first layer) to compensate for the increased stiffness. Accordingly, the results for $N_L = 2$ and $N_L = 3$ MLMs with $\lambda_{eff} = 1$ and $\lambda_{eff} = 2$, are provided in Fig. 17. The FFT amplitude results clearly show peak reduction at low frequencies, where amplitudes exceed 1 g only below 1.1 Hz, enlarging the protection range; instead, the responses are still above the DBE level in the low-frequency range. See (Fig. 18).

An overall comparison can be drawn between the single and the multi-layer configurations subjected to the bDBE-2 level. In this respect, the FRF results are normalised to the SLM configuration ($N_L = 1$, $d_Z = 18m$). Considering the SLM with inerters, the performance reduction above 1.4 Hz is evident, specifically around 2.2 Hz; conversely, there is an important improvement in the low frequency range. This also holds for the MLM with inerters; however, above 5 Hz, the MLM outperforms the SLM without inerters. Nonetheless, the results clearly show that the total height of MF is an important factor for performance.
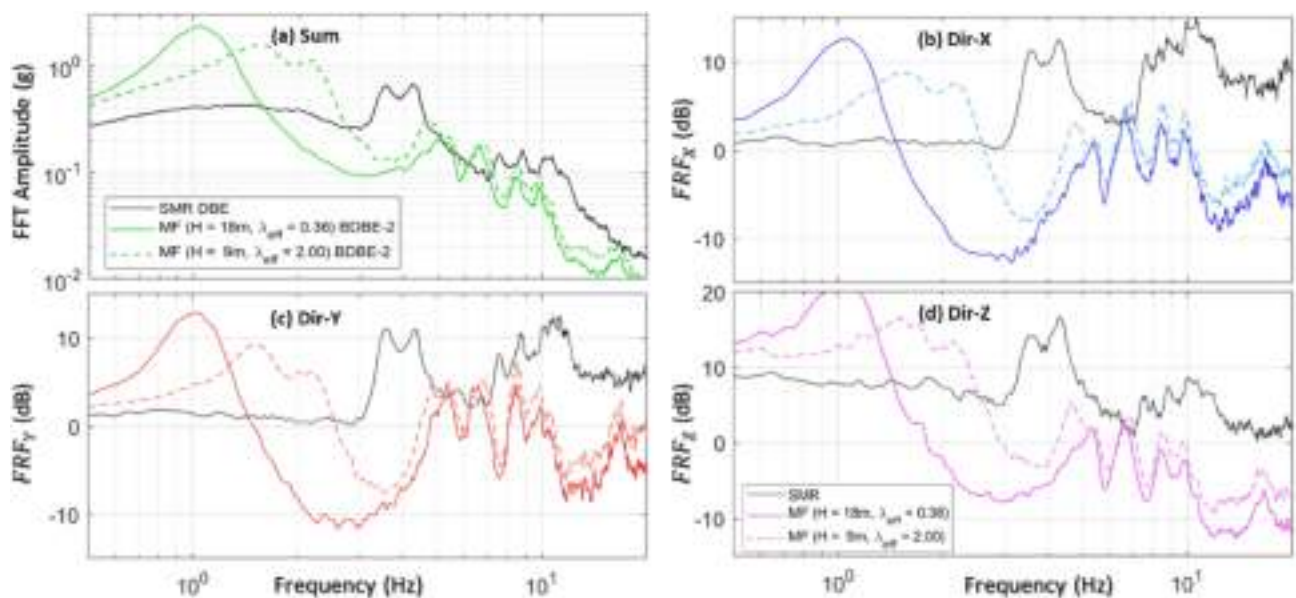

Fig. 15. (a) Averaged FFT amplitude and (b-d) FRF results for the middle node set of SMR-MF with and w/o inerters subjected to bDBE-2 triplets. The median of the average acceleration FRFs of middle set nodes for each direction is depicted. Black lines represent the SMR performance with a fixed base, whilst coloured represent the SMR equipped with MFs with different H and λ_{eff} parameters.
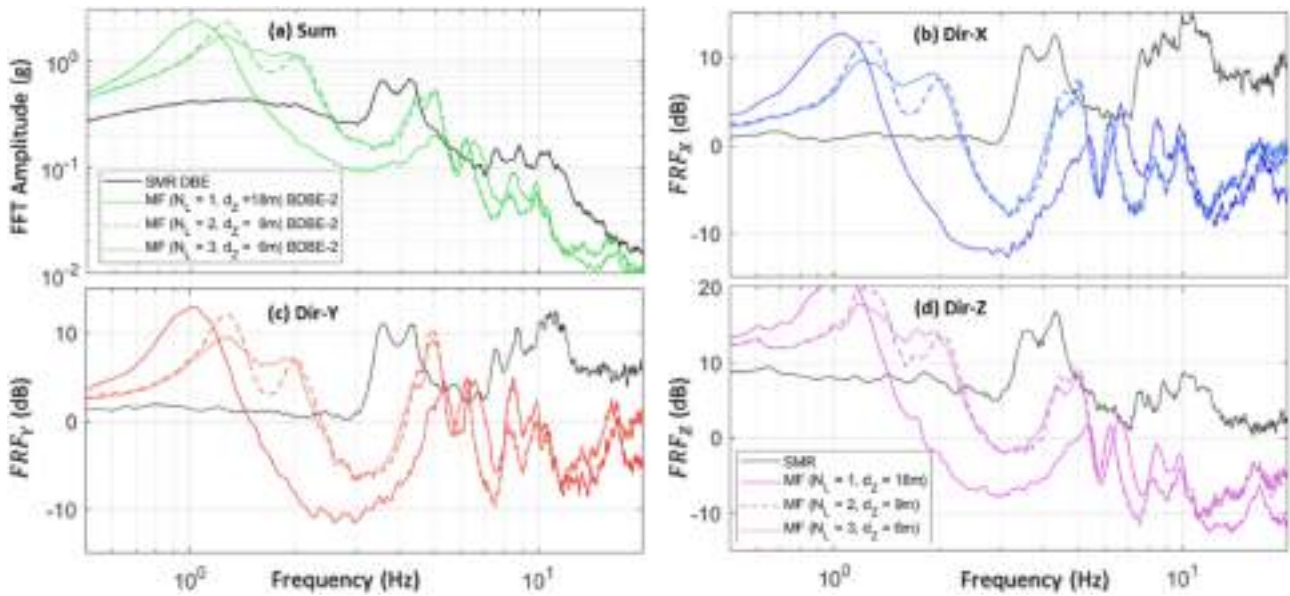
Fig. 16. (a) Averaged FFT amplitude and (b-d) FRF results for the middle node set of SMR-MF (with 1-, 2- and 3- layers) subjected to bDBE-2 triplets for each direction. Black lines represent the SMR performances, whilst coloured represent the SMR equipped with MF with single and multiple layers, respectively.
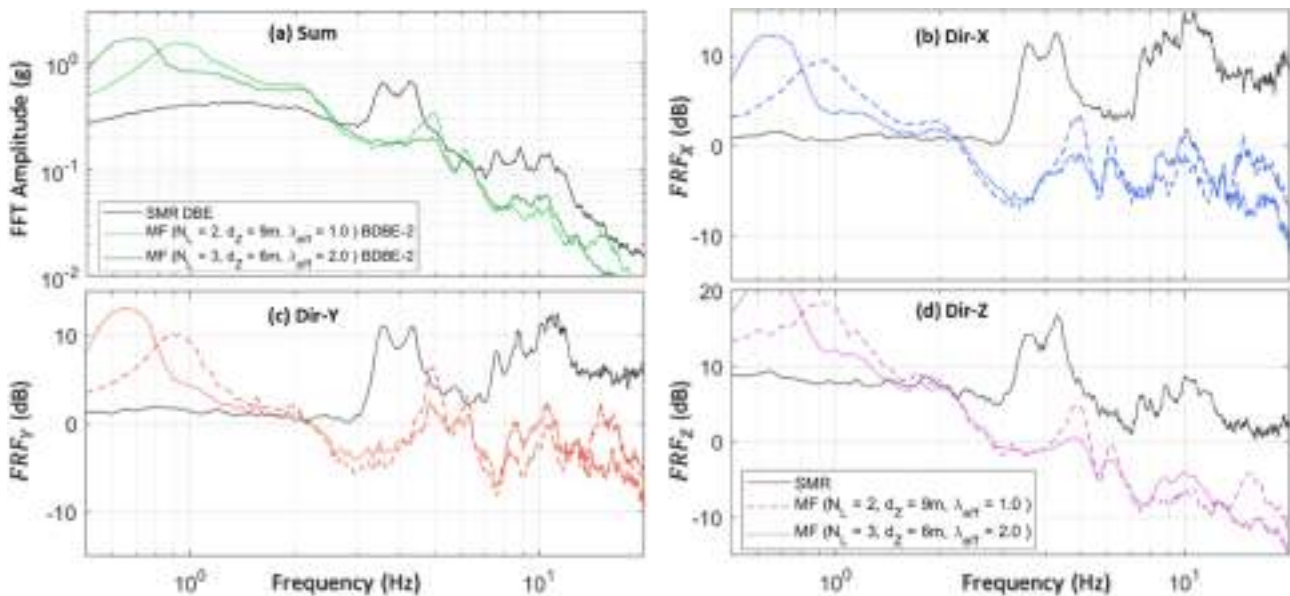

Fig. 17. (a) Averaged FFT amplitude and (b-d) FRF results for the middle node set of the SMR building and SMR-MF equipped with inerters subjected to bDBE-2 triplets. Black lines represent SMR performances, whilst coloured represent the SMR equipped with MF with 2 (dotted lines) and 3 (continued lines) layers, respectively.

7. Conclusions

This research has addressed the seismic protection of the Nuward™ SMR building through the introduction of metafoundations (MFs) grounded in the metamaterials concept. The primary goal was not only to mitigate seismic damages, but also to enhance the design standardisation of the SMR building. The study started with the employment of the FE model of the SMR building and, then, utilizing the Craig-Bampton mode synthesis technique, it established a low-fidelity representation. Both validation of the model's accuracy and its applicability has been achieved through the modal assurance criterion and modal orthogonality conditions.

The proposed MF modelling and its optimization have been extensively discussed, revealing intricate parameter selection requirements.

However, this complexity has also enabled the design flexibility and adaptability of MFs to project/site-specific demands. Then, the study has explored various design aspects including column sections, cell numbers, layer configurations, and layer heights. The conclusion was that as the number of cells increases, the horizontal flexibility increases, reducing the vertical flexibility and available resonator masses. Moreover, as the layer height increases, the overall MF performance increases; nonetheless, other constraints such as available under-structure space and cost still represent limitation factors.

To assess the MF performance and to ensure robustness beyond DBE and for more severe code-spectra scenarios, a new methodology for seismic triplets generation and selection has been presented. Ground motion models (GMMs) have been deployed to generate a suite of horizontal and vertical synthetic ground motions. To check and select code-
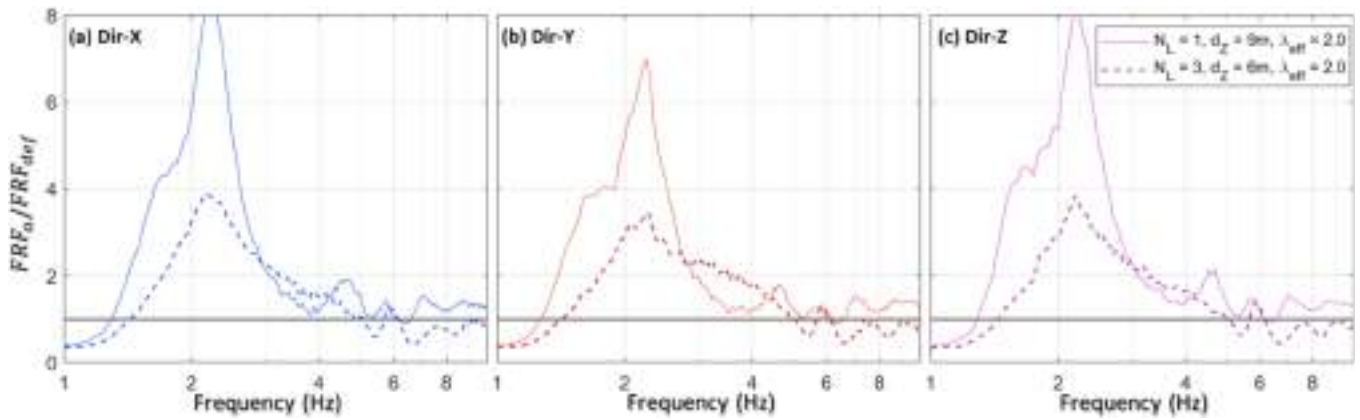
Fig. 18. Ratio of the FRFs for SLM equipped with inerters (NL = 1) and MLM with inerters (NL = 3), normalised to the case SLM without inerters (NL = 1, d_Z = 18 m). The FRF results correspond to the middle node set, with the SMR-MF subjected to the bDBE-2 triplets. Black lines represent the unit value for which values above one indicate a worse performance.

compliant seismic triplets, an algorithm for statistical independence based on the Hilbert-Schmidt criterion has been implemented, along with compatibility procedures. Specifically, above 3 Hz, where the SMR building modal mass participation is significant, time-history analyses based on triplets of accelerograms for DBE and beyond DBE conditions, have demonstrated the significant protective capabilities of MFs. Results indicated reduced peak responses and overall frequency domain responses, with attenuation at resonance frequencies of crucial structural and non-structural components.

To address limitations related to resonator masses, the study has introduced the novel concept of inerters applied to MFs. Specifically, MFs equipped with inerters exhibit substantial size reduction and allow their use with multiple layers for ultra-low frequency attenuation. In this respect, the research findings suggest that MFs meet the seismic protection requirements and positively contribute to the standardization process of SMR buildings. Moreover, MFs demonstrate their versatility to allow for the adoption of standard SMR buildings in locations with beyond design seismic conditions. Future research studies have to consider the experimental characterization of wire ropes or equivalent devices. Finally, the incorporation of both geometrical and mechanical randomness in the design and construction stages of MFs requires future studies.

CRediT authorship contribution statement

Tugberk Guner: Writing – original draft, Validation, Software, Methodology, Formal analysis, Conceptualization. **Chiara Nardin:** Writing – original draft, Validation, Methodology, Conceptualization. **Oreste S. Bursi:** Writing – review & editing, Supervision, Resources, Methodology, Conceptualization. **Silvano Erlicher:** Writing – review & editing, Resources, Conceptualization. **Alexandre Monteil:** Writing – review & editing, Resources.

Declaration of competing interest

The authors declare that they have no known competing financial interests or personal relationships that could have appeared to influence the work reported in this paper.

Data availability

The authors do not have permission to share data.

Acknowledgements

Appendix A. . Solution relevant to a periodic system

To provide clarity on LRMs introduced in Section 3, this part aims to elucidate the purpose and benefits of MFs through a simplified numerical lattice configuration, reduced to a single-axis motion. In this context, finite lattices with resonators, comprising 1 and 5 undamped cells were analyzed. Conducting a fixed amplitude frequency sweep, FRFs were calculated as the ratio of the last cell's displacement to the input which are presented in Fig. 4(c) where also the propagation of a system with periodic boundaries, i.e. infinitely many numbers of cells, are provided. More specifically, the propagation boundaries for the undamped periodic system were computed using the Floquet-Bloch theorem considering both spatial and temporal periodicity.

Basically, the Floquet-Bloch theorem is a mathematical tool used to analyze the behaviour of spatially periodic systems subjected to a periodic external perturbation where Bloch's theorem states that the wavefunctions in a periodic potential can be written as a product of a plane wave and a periodic function (Srikantha Phani and Hussein, 2017). On the other hand, the Floquet theory considers that if the Hamiltonian of the system is periodic in time, the solutions will exhibit periodic behaviour. Accordingly, in a periodic system, the displacement of the nth, $(n-1)^{th}$, and $(n+1)^{th}$ mass read, respectively,

$$x_n(t) = A_0 \cdot e^{-\omega t} x_{n\pm 1}(t) = A_0 \cdot e^{-\omega t} \cdot e^{\pm ikd} = A_0 \cdot e^{-\omega t \pm i\mu} \tag{14}$$

where ω is the wave frequency, $\mu = kd$ is the lattice constant (wave number x intercell distance), and A_0 is the propagating wave amplitude. Inserting

these equations into the system of EoMs, the dispersion relation, i.e. relation between wave number and frequency, can be obtained as follows:

$$\mu = k \cdot d = \arccos\left(1 - \frac{\omega^2}{2\omega_n^2}\left(1 + \frac{m_r\omega_r^2}{m_n(\omega_r^2 - \omega^2)}\right)\right) \tag{15}$$

The propagation boundaries can be obtained by solving (16) for $\mu = 0$ & $\mu = \pi$ and given as:

$$\frac{\omega_{UB}}{\omega_r} = \sqrt{\frac{(m_r + m_n)}{m_n}}, \frac{\omega_{LB}}{\omega_r} = \sqrt{\frac{4k_n}{(m_n + k_r + 4k_n)}} \tag{16}$$

where UB and LB correspond to the upper and lower boundaries of the propagation boundaries, respectively. Assuming the main cell characterization constant, it is clear that upper boundary frequency increases as resonator mass increases. However, the lower boundary (loosely) depends on resonator stiffness. The relevant dispersion curves are depicted in Figure 21.
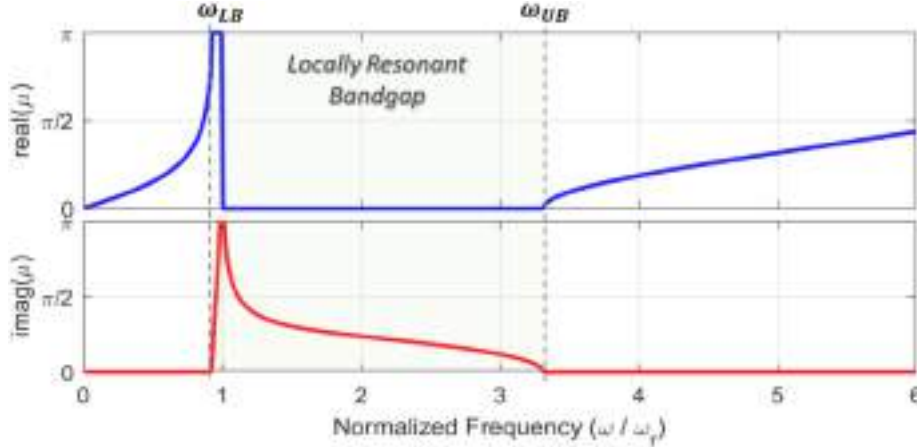

Fig. 19. Dispersion diagrams for the 1D periodic system relevant to the real and imaginary part of the propagation constant μ = kd.

Appendix B. . Code compliant physics-based synthetic triplets

The deployed GMM is the stochastic site-based developed by Rezaeian and Der Kiureghian, (2010a,2010b), described by the following equation:

$$a_g(t) = q(t, \widehat{\alpha})\left[\frac{1}{\sigma_f(t)}\int_{-\infty}^t h(t - \tau, \lambda(\tau))\omega(\tau)d\tau\right] \tag{17}$$

where $q(t, \widehat{\alpha})$ incorporates temporal non-linearities and $h(t - \tau, \lambda(\tau))$ spectral non-stationarities of the white-noise filtering and modulating generating process. Particularly, the time non-linearities is described by $\widehat{\alpha} = \arg\min_\alpha(|I_a(t_{45}) - \widehat{I}_a(t_{45})| + |I_a(t_{95}) - \widehat{I}_a(t_{95})|)$, where I_a is the Arias Intensity evaluated at t_{95} and t_{45}, i.e., at the instants at which the 95 % and 45 % of the total motion energy is reached, respectively. Conversely, the spectral component is described by $h(t - \tau, \lambda(\tau)) = f(\omega_f, \zeta_f)$, where $f(\omega_f, \zeta_f)$ is the impulse-response function IRF. Thus, the GMM is described by a total of six parameters: $\left\{I_a, D_{5-95}, t_{mid}, \omega_{mid}, \dot\omega_{mid}, \zeta_f\right\}$ which are strictly related to physical seismic motion characteristics:

(i) I_a, Arias intensity of the acceleration process (a measure of the total energy contained in the motion);
(ii) t_{45}, the time at which a 45 % level of the expected Arias intensity is reached (the time in the middle of the strong shaking phase);
(iii) D_{5-95}, the effective duration of the motion (related to the strong shaking phase of the time-history);
(iv) ω_{mid}, the filter frequency at t_{45};
(v) $\dot\omega$, the rate of change of the filter frequency with time;
(vi) ζ_f, the filter damping ratio assumed as a constant value.

To set the distribution of the parameters for the GMM, real seismic records were retrieved from the Engineering Strong Motion Database (Luzi et al., 2020). They respect the following criteria: (i) far-field events only, i.e. the Joyner-Boore R_{JB} distance > 20 km; (ii) normal fault only; (iii) shear wave V_{s30} velocity > 300 m/s, (soil type B); (iv) strong motions, i.e., PGA > 3 g (scaling until a factor of 5 was accepted). Thus, 7 different events made of two horizontal and one vertical component from 9 separated stations were selected. Table B.1 collects the real GMs and their feature selection; whilst Table B.2 reports the inferred marginal probability distribution on the real horizontal and vertical GMs dataset to assign to the parameters of the GMM. Moreover, Figure 20 showcases cross-correlation plots among the six physics-informed parameters of the GMM. Along the main diagonal, the marginal distributions of the parameters are reported as identified in Table 2. No strong correlations at all appear among the input parameters, neither for the horizontal nor vertical GMs.

Table B1
List of the selected real GMs and relevant features.

No. Station	No. event	Event Name	ID component#	Station	Scale Factor	PGA (m/s2)	Rjb (km)	Fault Mechanism	Vs30 (m/s)
1	1	Greece	GR-1995–0047 −1	PAT2	4.5	−3.99	49.80	Normal Fault	381
2	2	Friuli_1st_Shock	IT-1976–0002 −1	TLM1	1.3	−4.03	27.70	Normal Fault	458
3	3*	Irpinia	IT-1980–0012 −1	BGI	2.5	4.59	21.90	Normal Fault	498
4	3*	Irpinia	IT-1980–0012 −1	BGI	2.5	4.59	21.90	Normal Fault	498
5	3*	Irpinia	IT-1980–0012 −1	BGI	2.5	4.59	21.90	Normal Fault	498
6	4	Umbria Marche 2nd Shock	IT-1997–0006 −1	MTL	4.4	−4.67	27.00	Normal Fault	579
7	5	Umbria Marche 3rd Shock	IT-1997–0137 −1	NRC	3.5	−4.59	20.40	Normal Fault	498
8	6	Turkey	TK-1998–0063 −1	3301	4.9	−6.18	62.60	Normal Fault	367
9	7	Izmit	TK-1999–0077 −1	4106	2.1	5.49	46.00	Normal Fault	701

Table B2
Inferred marginal probability distribution on the real horizontal and vertical GMs.

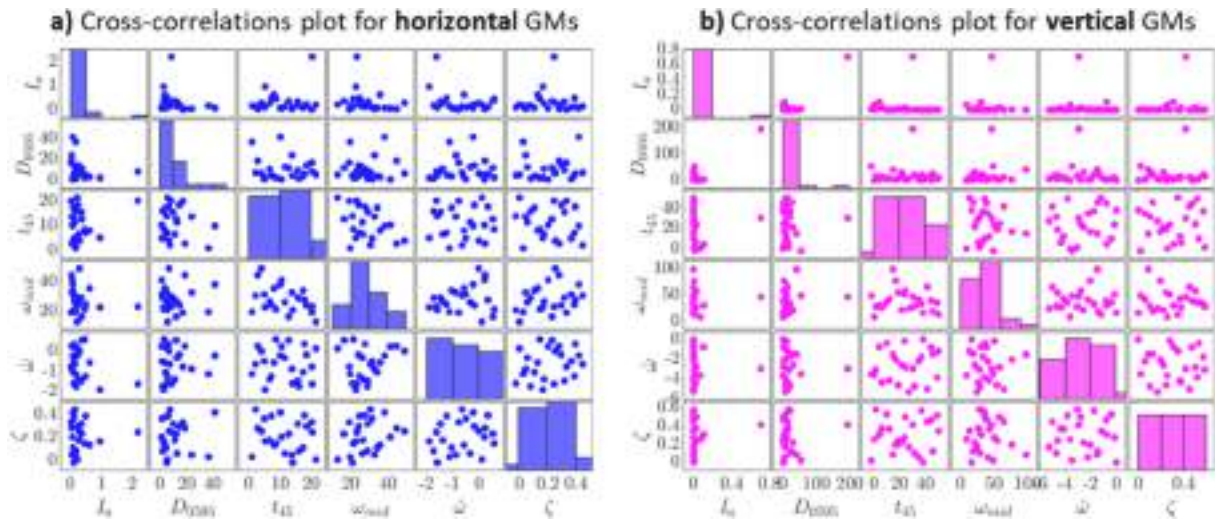| Index	Name	Type	Horizontal				Vertical			
			Parameters		Moments		Parameters		Moments	
1	I_a	Lognormal	−1.70	1.03	0.31	0.42	−5.74	2.27	0.04	0.55
2	t_{45}	Lognormal	2.04	0.92	11.69	13.46	2.43	1.03	19.20	26.29
3	D_{0595}	Uniform	0.82	22.02	11.42	6.12	−2.92	51.66	24.37	15.76
4	ω_{mid}	Gumbel	24.59	7.28	28.79	9.33	30.54	15.82	39.68	20.29
5	$\acute{\omega}$	Uniform	−1.93	0.68	−0.63	0.75	−5.36	0.20	−2.58	1.61
6	ζ	Uniform	−0.02	0.45	0.22	0.13	0.00	0.60	0.30	0.18

Fig. 20. Cross-correlations plot for the (a) horizontal and (b) vertical real GMs.

Next, two separated ensembles of 10^4 GMs for the horizontal and vertical components were generated. Figure 21 reports the acceleration spectra and the relevant statistics of the real and simulated GMs. Particularly, the dotted lines delimit the 5 % and 95 % quantiles; whilst the continued lines denote the mean of the real records and of the simulated synthetic ones. A good agreement was achieved. For the vertical case, in the long period range the upper bound of the simulated GMs is generally underestimating the spectral values regarding the real records.
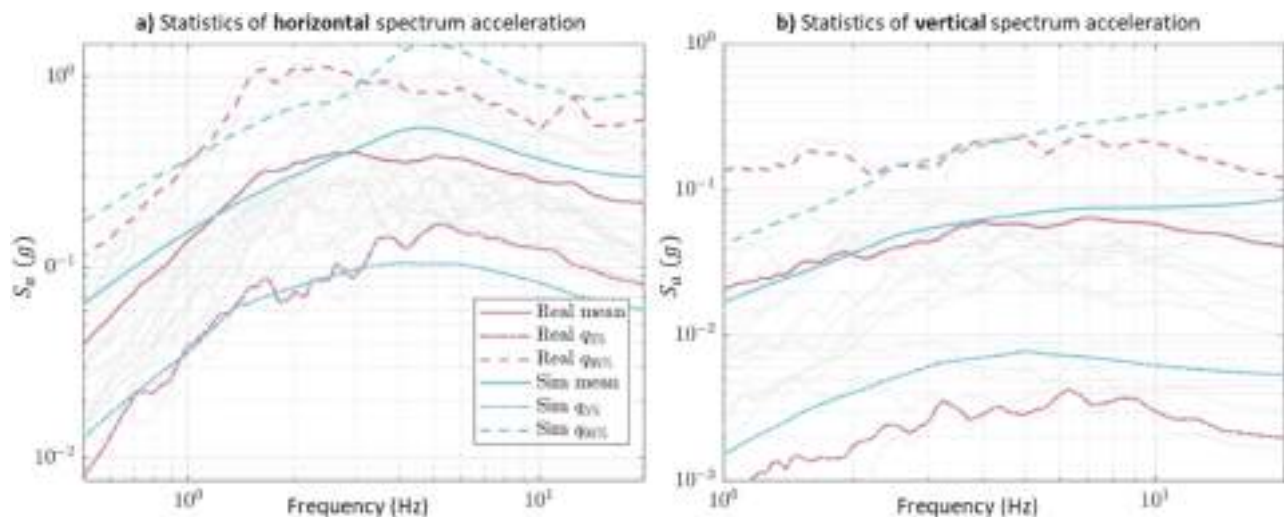
Fig. 21. (a)Horizontal and (b)Vertical acceleration spectra: statistics of the real and synthetic records.

References

Akkar, S., Sandikkaya, M.A., Ay, B.Ö., 2014. Compatible ground-motion prediction equations for damping scaling factors and vertical-to-horizontal spectral amplitude ratios for the broader European region. Bull. Earthq. Eng. 12, 517–547.

Alessandri, S., Giannini, R., Paolacci, F., Malena, M., 2016. Seismic retrofitting of an HV circuit breaker using base isolation with wire ropes. Part 1: preliminary tests and analyses. Eng. Struct. 98, 251–262.

Advanced Reactor Information System, ARIS (2023). International Atomic Energy Agency, https://aris.iaea.org/.

ASCE/SEI, (2016) Seismic Analysis of Safety-Related Nuclear Structures., Standard 4-16.

Basone, F., Wenzel, M., Bursi, O.S., Fossetti, M., 2019. Finite locally resonant Metafoundations for the seismic protection of fuel storage tanks. Earthq. Eng. Struct. Dyn. 48 (2), 232–252.

Bommer, J.J., Akkar, S., Kale, O., 2011. A model for vertical-to-horizontal response spectral ratios for Europe and the Middle East. Bull. Seismol. Soc. Am. 101, 1783–1806.

Bozorgnia, Y., Campbell, K., 2016. Ground motion model for the vertical-to-horizontal (V/H) ratios of PGA, PGV, and response spectra. Earthq. Spectra 32. https://doi.org/10.1193/100614EQS151M.

Brûlé, S., Enoch, S., Guenneau, S., 2020. Emergence of seismic metamaterials: current state and future perspectives. Phys. Lett. A 384 (1), 126034.

Bursi, O.S., Basone, F., Wenzel, M., 2021. Stochastic analysis of locally resonant linear and hysteretic metamaterials for seismic isolation of process equipment. J. Sound Vib. 510.

Cai, Z., Xie, W.-C., Pandey, M.D., Ni, S.-H., 2018. Determining seismic fragility of structures and components in nuclear power plants using multiple ground motion parameters – part I: methodology. Nucl. Eng. Des. 335, 195–201. https://doi.org/10.1016/j.nucengdes.2018.05.013.

Chen, M.Z.Q., Papageorgiou, C., Scheibe, F., Wang, F.C., Smith, M.C., 2009. The missing mechanical circuit element. IEEE Circuits Syst. Mag. 9 (1), 10–26.

Chopra, A. K., (2017), Dynamics of Structures.

Chwialkowski, K.P., Gretton, A., 2014. A kernel independence test for random processes. International Conference on Machine Learning. https://doi.org/10.48550/arXiv.1402.4501.

Cook, R.D., Malkus, D.S., Plesha, M.E., Witt, R.J., 2007. Concepts and Applications of Finite Element Analysis. John Wiley & Sons Inc, Hoboken, NJ, USA.

Craig Jr, R.R., Bampton, M.C., 1968. Coupling of substructures for dynamic analyses. AIAA J. 6 (7), 1313–1319.

CSA. 2010. Design procedures for seismic qualification of nuclear power plants. CSA N289.3-10 (Revised 2015), Canadian Standard Association.

Computers and Structures, Inc., CSI, (2022). SAP2000: Integrated Finite Element Analysis and Design of Structures, Version 23.3.1, software, Berkeley, CA.

Dalela, S., Balaji, P.S., Jena, D.P., 2022. A review on application of mechanical metamaterials for vibration control. Mech. Adv. Mater. Struct. 29 (22), 3237–3262.

De Domenico, D., Ricciardi, G., Zhang, R., 2020. Optimal design and seismic performance of tuned fluid inerter applied to structures with friction pendulum isolators. Soil Dyn. Earthq. Eng. 132, 106099.

Der Kiureghian, A., Rezaeian, S., 2010. Stochastic Modeling and Simulation of Ground Motions for Performance-Based Earthquake Engineering. Tech. Rep. Center College of Engineering University of California, Berkeley.

Di Maio, F., Bani, L., Zio, E., 2023. Seismic resilience assessment of small modular reactors by a three-loop monte carlo simulation. Nucl. Eng. Des. 410, 112385.

European Committee for Standardization, (2004), Design of composite steel and concrete structures. Part 1-1: General rules and rules for buildings. Eurocode 4-1-1, CEN/TC 250, Brussels.

European Committee for Standardization, (2004), Design of structures for earthquake resistance. - Part 1: General rules, seismic actions and rules for buildings. Eurocode 8-1, CEN/TC 250, Brussels.

European Committee for Standardization, (2005), Design of composite steel and concrete structures. Part 1-2: General rules - Structural fire design regulation. Eurocode 4-1-2, CEN/TC 250, Brussels.

European Committee for Standardization, (2005), Design of steel structures. Part 1-1: General rules and rules for buildings. Eurocode 3-1-1, CEN/TC 250, Brussels.

Franchini, A., Bursi, O.S., Basone, F., Sun, F., 2020. Finite locally resonant metafoundations for the protection of slender storage tanks against vertical ground accelerations. Smart Mater. Struct. 29 (5) https://doi.org/10.1088/1361-665X/ab7e1d.

Fukasawa, T., Okamura, S., Somaki, T., Miyagawa, T., Uchita, M., Yamamoto, T., Watakabe, T., & Fujita, S., (2019), Research and development of three-dimensional isolation system for sodium-cooled fast reactor: Part 4 - proposal of optimal combination method for disc spring units and newly friction model for sliding elements. American Society of Mechanical Engineers, Pressure Vessels and Piping Division, PVP, vol. 8.

Gulerce, Z., Abrahamson, N.A., 2011. Site-specific design spectra for vertical ground motion. Earthq. Spectra 27, 1023–1047.

Guner, T., Bursi, O.S., Erlicher, S., 2022. Optimization and performance of metafoundations for seismic isolation of small modular reactors. Comput. Aided Civ. Inf. Eng. https://doi.org/10.1111/mice.12902.

IAEA, International Atomic Energy Agency, (2016) Design Safety Considerations for Water Cooled Small Modular Reactors Incorporating Lessons Learned from the Fukushima Daiichi Accident. IAEA-TECDOC-1785.

IAEA, International Atomic Energy Agency, (2020) Advances in Small Modular Reactor Technology Developments.

Japan Electric Association, (2013). Technical guidelines on seismic base isolated system for structural safety and design of nuclear power plants. JEAG 4614-2013, Japan.

Ji, J.C., Luo, Q., Ye, K., 2021. Vibration control based metamaterials and origami structures: a state-of-the-art review. Mech. Syst. Sig. Process. 161, 107945.

La Salandra, V., Wenzel, M., Bursi, O.S., Carta, G., Movchan, A.B., 2017. Conception of a 3D metamaterial-based foundation for static and seismic protection of fuel storage tanks. Front. Mater. 4, 30.

Liu, C., Chen, L., Lee, H.P., Yang, Y., Zhang, X., 2022. A review of the inerter and inerter-based vibration isolation: theory, devices, and applications. J. Franklin Inst.

Lloyd, C.A., Roulstone, T., Lyons, R.E., 2021. Transport, constructability, and economic advantages of SMR modularization. Prog. Nucl. Energy 134, 103672.

Luzi, L., Lanzano, G., Felicetta, C., D'Amico, M.C., Russo, E., Sgobba, S., Pacor, F., ORFEUS Working Group 5 (2020). Engineering Strong Motion Database (ESM) (Version 2.0). Istituto Nazionale di Geofisica e Vulcanologia (INGV). https://doi.org/10.13127/ESM.2.

Ma, R., Bi, K., Hao, H., 2021. Inerter-based structural vibration control: a state-of-the-art review. Eng. Struct. 243, 112655.

Ma, G., Sheng, P., 2016. Acoustic metamaterials: from local resonances to broad horizons. Sci. Adv. 2 (2), e1501595.

Malhotra, P.K., Wenk, T., Wieland, M., 2000. Simple procedure for seismic analysis of liquid-storage tanks. Struct. Eng. Int. 10 (3), 197–201.

Marian, L., Giaralis, A., 2014. Optimal design of a novel tuned mass-damper-inerter (TMDI) passive vibration control configuration for stochastically support-excited

structural systems. Probab. Eng. Mech. 38, 156–164. Molina-Cristobal, A., Papageorgiou, C., Parks, G. T.

The MathWorks, Inc. (2022). MATLAB (Version 2021a) [Computer software]. https://www.mathworks.com/.

Medel-Vera, C., Ji, T. (2015). Seismic protection technology for nuclear power plants: a systematic review. Journal of Nuclear Science and Technology (Vol. 52, Issue 5, pp. 607–632). Taylor and Francis Ltd. https://doi.org/10.1080/00223131.2014.980347.

Mignacca, B., Locatelli, G., Sainati, T., 2020. Deeds not words: barriers and remedies for small modular nuclear reactors. Energy 206, 11813. https://doi.org/10.1016/j.energy.2020.118137.

Mu, D., Shu, H., Zhao, L., An, S., 2020. A review of research on seismic metamaterials. Adv. Eng. Mater. 22, 1901148. https://doi.org/10.1002/adem.201901148.

Najafijozani, M., Becker, T.C., Konstantinidis, D., 2020. Evaluating adaptive vertical seismic isolation for equipment in nuclear power plants. Nucl. Eng. Des. 358.

Newmark, N.M., 1959. A method of computation for structural dynamics. J .Eng. Mech. Div. 85 (EM3), 67–94.

Ni, S.-H., Xie, W.-C., Pandey, M.D., 2011. Tri-directional spectrum-compatible earthquake time-histories for nuclear energy facilities. Nucl. Eng. Des. 241 (8), 2732–2743.

Nielsen, G., Rees, S., Zekioglu, A., Sarebanha, A., Biscombe, L., Shao, B., Dong, B. (2020). A 3-D seismic isolation system to protect the Loma Linda University Hospital from near-fault earthquakes. In Proceedings of 17WCEE, Sep 2020, vol. 17. 2020.

Parsi, S.S., Lal, K.M., Kosbab, B.D., Ingersoll, E.D., Shirvan, K., Whittaker, A.S., 2022. Seismic isolation: a pathway to standardized advanced nuclear reactors. Nucl. Eng. Des. 111445.

Pietrosanti, D., De Angelis, M., Giaralis, A., 2021. Experimental seismic performance assessment and numerical modelling of nonlinear inerter vibration absorber (IVA)-equipped base isolated structures tested on shaking table. Earthq. Eng. Struct. Dyn. 50 (10), 2732–2753.

Rezaeian, S., Der Kiureghian, A., 2010. Simulation of synthetic ground motions for specified earthquake and site characteristics. Earthq. Eng. Struct. Dyn. https://doi.org/10.1002/eqe.997.

Schellenberg, A.H., Sarebanha, A., Schoettler, M.J., Mosqueda, G., Benzoni, G., Mahin, S. A., (2015), Hybrid Simulation of Seismic Isolation Systems Applied to an APR-1400 Nuclear Power Plant, PEER Report 2015/05.

Smith, M.C. (2002). Synthesis of mechanical networks: the inerter. Proceedings of the 41st IEEE Conference on Decision and Control, 2002., 2, 1657-1662 vol.2.

Srikantha Phani, A., Hussein, M.I. (Eds.), 2017. Dynamics of Lattice Materials. Wiley-Blackwell.

Stevenson, J.D., 2014. Summary of the historical development of seismic design of nuclear power plants in Japan and in the US. Nuclear Eng. Des. 269, 160–164.

Sugimura, Y., Goto, W., Tanizawa, H., Saito, K., Nimomiya, T. (2012, September). Response control effect of steel building structure using tuned viscous mass damper. In Proceedings of the 15th world conference on earthquake engineering (Vol. 9, pp. 24-28).

U.S. Nuclear Regulatory Commission (1978). NUREG/CR-0098, Development of criteria for seismic review of selected nuclear power plants, Washington, DC.

U.S. Nuclear Regulatory Commission (2007), Regulatory guide 1.61: damping values for seismic design of nuclear power plants, Washington, DC.

U.S. Nuclear Regulatory Commission (2015), NUREG/CR-7193, Evaluations of NRC Seismic-Structural Regulations and Regulatory Guidance, and Simulation-Evaluation Tools for Applicability to Small Modular Reactors (SMRs), Washington, DC.

Upadhyay, A.K., Jain, K., 2003. Modularity in nuclear power plants: a re-view. J. Eng., Desig. Tech. 14 (3), 526–542.

U.S. Nuclear Regulatory Commission, 2014. Regulatory Guide 1.60, "Design response spectra for seismic design of nuclear power plants," Rev. 2, Nuclear Regulatory Commission, Washington, D.C.

U.S. Nuclear Regulatory Commission, 2014. Standard review plan-seismic design parameters. SRP 3.7.1. U.S, Nuclear Regulatory Commission, Washington D.C.

Veletsos, A.S., Tang, Y. (1986). Dynamics of vertically excited liquid storage tanks. J. Struct. Eng., 112(6), 1228–1246.https://doi.org/10.1061/(ASCE)0733-9445(1986)112:6.

Watanabe, Y., Ikago, K., Inoue, N., Kida, H., Nakaminami, S., Tanaka, H., Saito, K. (2012, September). Full-scale dynamic tests and analytical verification of a force-restricted tuned viscous mass damper. In 15th World Conference on Earthquake Engineering. Lisbon, Portugal.

Witarto, W., Wang, S.J., Yang, C.Y., Wang, J., Mo, Y.L., Chang, K.C., Tang, Y., 2019. Three-dimensional periodic materials as seismic base isolator for nuclear infrastructure. AIP Adv. 9 (4).

Wood, J., 2008. The top ten advances in materials science. Mater. Today 11 (1–2), 40–45.

Wu, X., Su, Y., Shi, J., 2020. In-plane impact resistance enhancement with a graded cell-wall angle design for auxetic metamaterials. Compos. Struct. 247, 112451.

Yang, L., Xie, W.C., Xu, W., Ly, B.L., Wang, H., Meng, Q., 2022. Directional components of a seismic design accelerogram. J. Earthq. Eng. 26 (11), 5573–5591.

Zeighami, F., Palermo, A., Marzani, A., 2021. Rayleigh waves in locally resonant metamaterials. Int. J. Mech. Sci. 195, 106250.

Zhao, C., Yu N., Peng, T., Lippolis, V., Corona, A., Mo, Y.L., (2019), Study on the dynamic behavior of isolated AP1000 NIB under mainshock-aftershock sequences, Progress in Nuclear Energy, September.